The adjoint method of data assimilation used operationally for shelf circulation

David A. Griffin[1] and Keith R. Thompson

Oceanography Department, Dalhousie University, Halifax, Nova Scotia, Canada

Abstract. A real-time shelf circulation model with data assimilation has been successfully used, possibly for the first time, on the outer Nova Scotian Shelf. The adjoint method was used to infer the time histories of flows across the four open boundaries of a 60 km × 60 km shallow-water equation model of Western Bank. The aim was to hindcast and nowcast currents over the bank so that a patch of water (initially 15 km in diameter) could be resampled over a 3-week period as part of a study of the early life history of Atlantic cod. Observations available in near real time for assimilation were from 14 drifting buoys, 2 telemetering moored current meters, the ship's acoustic Doppler current profiler and the local wind. For the postcruise hindcasts presented here, data from two bottom pressure gauges and two more current meters are also available. The experiment was successful, and the patch was sampled over a 19-day period that included two intense storms. In this paper we (1) document the model and how the data are assimilated, (2) present and discuss the observations, (3) demonstrate that the interpolative skill of the model exceeds that of simpler schemes that use just the current velocity data, and (4) provide examples of how particle tracking with the model enables asynoptically acquired data to be displayed as synoptic maps, greatly facilitating both underway cruise planning and postcruise data analysis. An interesting feature of the circulation on the bank was a nearly stationary eddy atop the bank crest. Larvae within the eddy were retained on the bank in a favorable environment until the onset of the storms. The variable integrity of the eddy may contribute to fluctuations of year-class success.

Introduction

"Data assimilation" is a term coming into use in oceanography to cover a wide range of methods of systematically reconciling hydrodynamic models with observations. The present paper discusses an application of a form of variational data assimilation known as the adjoint method [*Talagrand and Courtier*, 1987]. The method is thus named because the adjoint of the model equations is used to compute the directions in which unknown model parameters should be adjusted to achieve a better fit of the model to the data. Used iteratively with a gradient-descent algorithm, the method allows unknown model parameters to be inferred from the data.

Thacker and Long [1988] were among the first to consider an oceanographic application of the adjoint

method and provide an excellent introduction to the basic concepts and how it relates to other methods. They performed a series of identical twin experiments to demonstrate how observations of surface elevation in addition to wind stress might be used to recover the state of a simple equatorial ocean model. Other users of the adjoint method include *Panchang and O'Brien* [1989], who inferred the bottom friction coefficient from experimental channel flow data; *Smedstad and O'Brien* [1991], who assimilated real sea level observations at three equatorial Pacific stations into a reduced gravity model; *Moore* [1991], who inferred corrections to the initial conditions of a quasi-geostrophic (QG) model by assimilating Geosat altimeter data; *Das and Lardner* [1991] and *Lardner et al.* [1993], who inferred the bottom friction coefficient and bathymetric corrections in a tidal model; *Tziperman et al.* [1992a,b] , who discuss the difficulties of assimilating simulated and real data of various types into a simplified primitive equation multilayer model; and *Schlitzer* [1993], *Nechaev and Yaremchuk* [1994] and *Schiller* [1995], who inferred the mean circulation of the Atlantic from hydrographic data. Two recent applications of the adjoint method to infer open boundary conditions are those of *Seiler* [1993], who assimilated simulated satellite data into a QG model; and *Lardner* [1993], who assimilated tide

[1]Now at Division of Oceanography, Commonwealth Scientific and Industrial Research Organisation, Hobart, Tasmania, Australia.
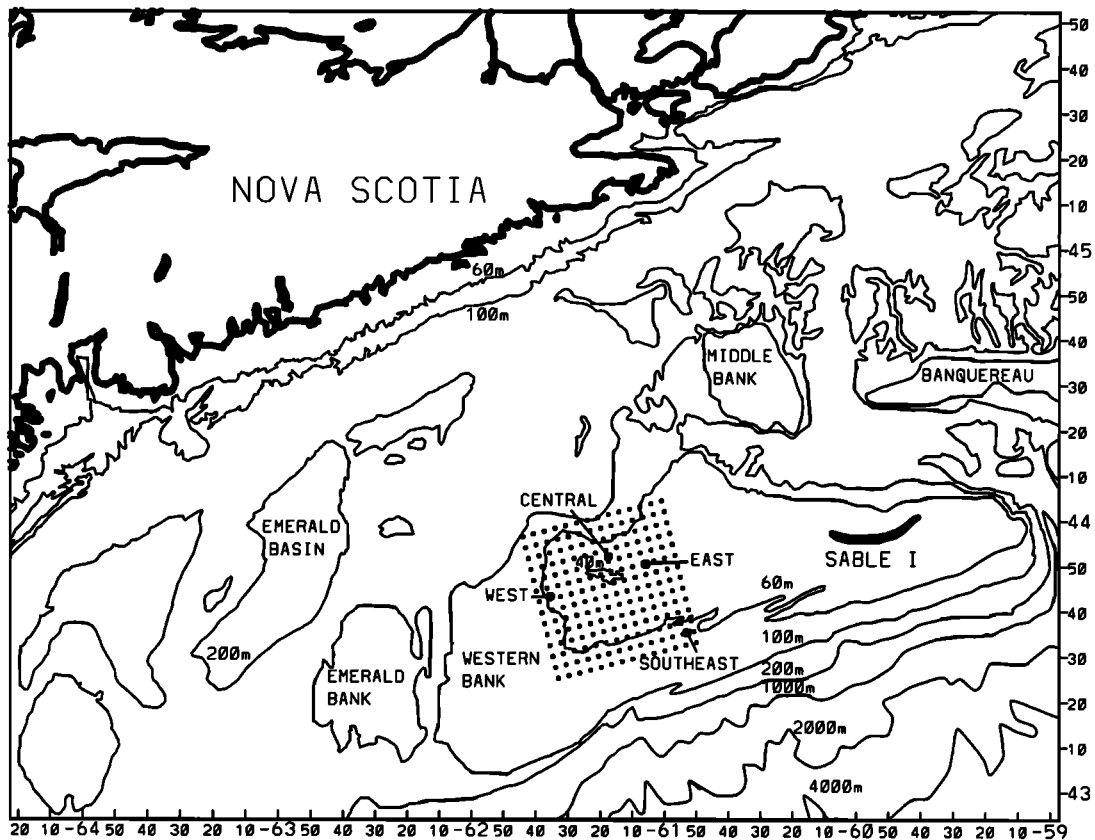
Figure 1. Bathymetric map of the Scotian Shelf, showing the locations of four current meter moorings and model pressure grid nodes.

gauge data into a regional tidal model. *Heemink and Metzelaar* [1995], in a novel application of the adjoint method in conjunction with a Kalman filter, assimilate sea level data into a storm surge model. The adjoint method has also been used to analyze perturbation growth in oceanic flows [*Farrell and Moore*, 1992; *Moore and Farrell*, 1993]. *Ghil and Malanotte-Rizzoli* [1991] give a comprehensive review of data assimilation in meteorology and oceanography.

Our work is part of a multidisciplinary study of the early life history of Atlantic cod (*Gadus morhua*). The Nova Scotian stock has an important spawning ground on Western Bank on the outer shelf (Figure 1). The aim of the study was to determine whether the larvae that survived the conditions prevailing during the study had any characteristics to distinguish them from nonsurvivors. Preliminary results are given by *Taggart et al.* [1995] and *S.E. Lochmann et al.* (Temporal changes of lipid class composition and survival of a cohort of cod larvae, submitted to *Canadian Journal of Fisheries and Aquatic Sciences*, 1995).

To be successful, the study had to be conducted in as close as possible to a Lagrangian framework, lest spatial gradients of properties of the population appear as temporal. The usual approach to tracking a parcel of water in real time is to follow drogued buoys, but telemetering drifters are expensive, are subject to

windage and wave drag, and tend to converge at fronts. Instead, we used current velocity observations from current meters, drifters, and a vessel-mounted acoustic Doppler current profiler (ADCP) to map out the time dependent flow field in the study region. We then tracked patches of water using this flow field. In essence, the problem was how to infer a flow field history from a few scattered observations. We assumed that a simple but fine resolution (4.5-km grid) hydrodynamic model of the circulation in the approximately 60 km × 60 km study region (see Figure 1) could be made to reproduce the observations if forced by the local wind and appropriately at the open boundaries. To infer the boundary forcing, we used the adjoint method of data assimilation.

In the following sections we present the model and discuss the method of data assimilation. Details of the adjoint model equations are included in the appendix. The cruise data and results of assimilation are then presented, with some examples given of how the model was used to help interpret other data. A summary and discussion of some technical issues concerning data assimilation conclude the paper. Several aspects of the work reported here are only covered briefly in order not to duplicate the more complete technical discussion by *K.R. Thompson and D.A. Griffin* (Circulation on the outer shelf: construction and validation of a limited-

area model with open boundary conditions inferred by data assimilation, manuscript in preparation, 1995) (hereinafter referred to as TG), who assimilate a different data set to a similar model.

A Model With Data Assimilation

There are many ways of fitting a model to data, ranging in complexity from simple nudging to variational methods such as ours. To fit the dependent variables of our model to the data, we only make adjustments to the independent or "control" variables, such as the initial and boundary conditions. This is known as a strong constraint [Sasaki, 1970] method because the model equations are obeyed exactly. The number of control variables is large, and the influence of each on the goodness of fit is through all the model equations, presenting quite a formidable inverse problem. TG discuss the problem in terms of regression and show how it can, in principle, be solved directly but that to do so would be computationally prohibitive. Instead, we find the minimum of the cost function (which measures both the misfit to the observations and various other properties, such as the total model volume flux) by computing its gradient with respect to the control variables and stepping downhill using a linear conjugate gradient descent method [Gill et al., 1981]. The appendix outlines how an adjoint model is run backward in time to compute the gradients. We now discuss the forward model, its control variables, and the cost function.

The Forward Model

We are primarily interested in modeling the velocity field at 20 m, where most of the cod larvae are found. We break the velocity u, v (along x, y) and pressure p fields at 20 m into two noninteracting components as follows: (1) a slowly evolving geostrophic component (u_d, v_d, p_d), associated with the density field and (2) a barotropic component (u_b, v_b, p_b) due to local (wind) and remote (wind, tidal, and other) forcing.

The geostrophic component is isolated from the remaining variability because we observed a strong current that was clearly associated with the density field and not constrained to follow isobaths (see TG and below). The slow time evolution of (u_d, v_d, p_d) was judged not to be modelable with a prognostic density equation, so we take a diagnostic approach and assume perfect geostrophy at any time t and express the velocities in terms of the pressure

$$- f v_d + \frac{1}{\rho} \frac{\partial p_d}{\partial x} = 0 \qquad (1)$$

$$f u_d + \frac{1}{\rho} \frac{\partial p_d}{\partial y} = 0. \qquad (2)$$

Here f is the (uniform) Coriolis parameter. We expand the pressure in terms of S_d basis functions ϕ with coefficients that vary piecewise linearly between values defined at control times T. Specifically, we use Legendre

polynomials of order 1 to 4 (so $S_d = 14$) and define the control variables α at intervals of $\Delta T_d = 8$ days which is long enough to be consistent with the omission of the acceleration terms in (1) and (2) but short enough to allow advection of the density field by storms to be adequately reproduced. Hence we write

$$p_d(x, y, t) = \sum_{s=1}^{S_d} \sum_{T=T1}^{T2} \alpha_s^T \omega(t - T) \phi_s(x, y) \qquad (3)$$

where the ω weighting function performs the linear interpolation between the two nearest control times T1 and T2.

The barotropic component obeys

$$\frac{\partial u_b}{\partial t} - f v_b + \frac{1}{\rho} \frac{\partial p_b}{\partial x} + \frac{C_D v^* u_b}{h} - \frac{\tau^x}{\rho h} = 0 \qquad (4)$$

$$\frac{\partial v_b}{\partial t} + f u_b + \frac{1}{\rho} \frac{\partial p_b}{\partial y} + \frac{C_D v^* v_b}{h} - \frac{\tau^y}{\rho h} = 0 \qquad (5)$$

$$\frac{1}{\rho g} \frac{\partial p_b}{\partial t} + \frac{\partial h u_b}{\partial x} + \frac{\partial h v_b}{\partial y} = 0 \qquad (6)$$

where u_b and v_b are averaged over the local depth h, ρ is the average density, and g is the acceleration due to gravity. Superscripts x and y distinguish components of the wind stress τ. We have not attempted to infer the bottom drag coefficient C_D from the data by treating it as a control variable but, instead, set it to 1.5×10^{-3}; see the Discussion section. A more significant advance is to set the linearizing speed v^* to $(u_p^2 + v_p^2)^{1/2}$ instead of a constant, where subscript p denotes prescribed values of u_b, v_b obtained from a completed assimilation run (which might have had $v^* = 0.2$ m s^{-1}). Note that the current due to the density field is much weaker than the barotropic (e.g., tidal) currents at the bottom and is not included in v^*.

The model is discretized on a 14 × 14 Arakawa C grid ($\Delta x = 4588$ m) with the four open boundaries at the boundary-normal velocity grid points. Explicit time stepping is used, with $\Delta t = \Delta x / [\gamma (gH)^{1/2}]$ where $\gamma > 2^{1/2}$ in order to satisfy the Courant-Friedrichs-Lewy condition. The pressure field for the new time step is updated first by applying the continuity equation to the velocity field at the old time. Then the interior velocity grid points are updated using the momentum equations. The boundary velocities are given in terms of S control variables at each control time T and the pressure field. For example, at the left open boundary

$$h u_b(y, t) = \sum_{s=1}^{S} \sum_{T=T1}^{T4} l_s^T \kappa(t - T) \chi_s(y) - h \frac{p_b(y, t) \cos \theta}{\rho (gh)^{1/2}} \qquad (7)$$

where κ is a weighting function to perform quadratic interpolation between the four nearest control times T1 to T4 and χ is a set of basis functions evaluated along the boundary.

The first term on the right-hand side of (7) represents the component of the boundary velocity that is inferred by data assimilation. Why the need for κ and χ?
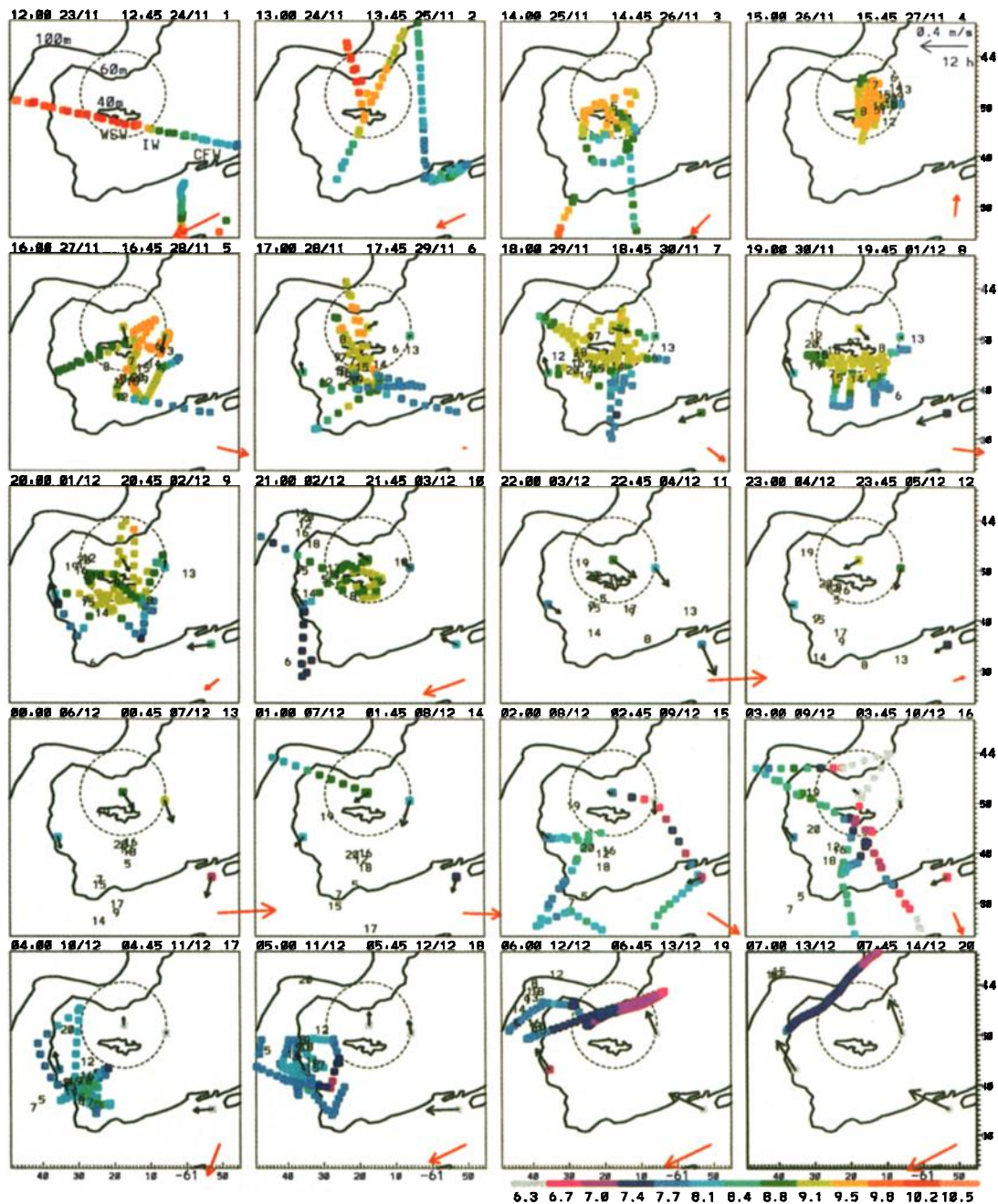
Plate 1. Cruise data by 25-hour panels (UT interval shown). Each panel shows along-track sea surface temperature 15-min means color-coded according to the scale shown, 25-hour-mean currents at the four 20 m current meters as black arrows scaled to represent 12 hours' advection (scale at top right), 25-hour-mean temperatures at the four 20 m current meters as the color of the arrow base, 25-hour-mean wind velocity as a red arrow at the bottom right of each panel, reduced to 3%, and drifter positions at the end of the 25 hours, indicated by symbols 5 to 9 and 12 to 20.

The total number of unknowns to be estimated (initial velocity and pressure fields, plus normal velocities at 14 points around the four sides every 1.25 min) is much greater than the number of observations, so the problem is grossly underdetermined if all unknowns are independent control variables. Two methods (see Discussion) are commonly used to guarantee a unique solution, and we use both. For the model runs presented here we find $S = 2$ [$\chi_1(y) = 1$, $\chi_2(y) = y$] and a control time step of $\Delta T = 90$ min gives sufficient degrees of freedom to adequately fit the data, while drastically reducing the number of unknowns. If more spatial structure in the flow is desired, we include a Gaussian (to put additional structure mainly near the center of

the boundary) or one or two orthogonal sinusoids or Legendre polynomials.

We have not experimented with expressing the initial conditions in terms of basis functions but, instead, prefer to set them to zero and start the model thirteen 90-min control time steps earlier than the first observation, thus requiring an additional $13 \times 4 \times S = 104$ extra control variables for the four boundaries, but saving $14 \times 14 + 14 \times 15 + 15 \times 14 = 616$ unknowns required to specify the initial conditions of the p, u and v grids. One reason for this choice is that the small size of the model's domain implies a fairly short spin-up period and, since it took several days before all the instruments were deployed, the model's state is poorly constrained by the data during the first few days, especially at the initial instant. Another reason is that reparameterizing the initial conditions while still guaranteeing dynamic balance is not straightforward. The boundary control variables are also poorly determined at the end of the integration because the number of instruments gradually goes to zero as they were retrieved or left the model domain; but even if the integration is halted when all instruments are deployed, the time taken for information to propagate in from the boundaries to the instrument locations causes the final control variables to be poorly determined (O. Talagrand, personal communication, 1994), causing slow convergence of the assimilation. Convergence is guaranteed by the second method of ensuring that the inverse problem is well determined, namely, addition of other penalty terms to the cost function (see below), which drives ill-determined control variables (or their gradients) to zero.

Note that the control variables are the boundary fluxes rather than velocities and that only χ_1 has a nonzero integral along the boundary (see discussion of (7)). This ensures that only one control variable per boundary (per ΔT) influences the model's mass budget, which helped cure a problem of slow convergence that arose when we started to assimilate bottom pressure data as well as velocities. Another consequence of defining the control variables in terms of the volume flux is that additional structure of the velocity field is due to topographic variability along the boundary.

The second term of (7) represents the component of the boundary velocity associated with the radiation of gravity wave energy. A problem encountered during model development was that basin seiche modes (with no flux through the boundaries) were excited, leading to very slow convergence of the assimilation scheme. The problem was that the seiche periods of the model domain were similar to the 90-min interval between control variables, making the motions difficult to control by adjusting the control variables. Penalization of the high frequency motions [Zou et al., 1992] was therefore ineffective. Our variation of the standard Reid and Bodine [1968] scheme is the inclusion of the $\cos\theta$ factor, where θ is the angle of incidence at the boundary of waves emanating from the center of the model domain. Tests showed this variation to be more effective than

the standard scheme which is unphysical at the corners of a square domain. Note that (7) assumes u and p are colocated which is not the case on a C grid. We use the nearest p grid point as if it were at the boundary.

The barotropic model is thus similar to a very basic storm surge model for shallow seas, except that its performance when compared with observations is not limited by the usual open boundary problems, one of which is how to allow outgoing disturbances to pass unreflected through the boundary. Chapman [1985] and Røed and Cooper [1987] compared several radiation schemes, all of which have problems radiating at least one type of disturbance. Models intended for realistic simulations face a second problem of how to represent 'unknown incoming disturbances. Both problems are solved by our approach of inferring the boundary conditions from interior observations, but, of course, the method depends on availability of interior observations.

The two model components are fit simultaneously to the data. The correct partitioning of the observed current variance to the appropriate component is less straightforward to achieve for the present data set than it is for TG. The problem is that we rely on topographic steering at low frequency of barotropic currents to distinguish the two model components, while the April data of TG include many conductivity-temperature-depth (CTD) casts which yield estimates of the dynamic height which are fitted only by p_d.

The major difference between the present model and that of TG is in how the wind-driven component of the current is modeled. We have chosen to include the wind stress in the depth-averaged shallow-water equations to account for the effects of local wind forcing, leaving the boundary conditions (which are inferred by data assimilation) to reproduce the effects of remote wind forcing. TG, on the other hand, make a three-way decomposition of the total velocity, including a separate component for the wind-driven current which they model as a uniform slab following Pollard and Millard [1970]. Their approach is appropriate for modeling the currents in April 1992 when weaker winds lead to the Ekman layer being less than the water depth. During the November-December 1992 period discussed here, however, storm force winds lead to the Ekman layer exceeding the 36-m to 95-m water depths within the model's domain, so topographic influences on the locally wind-driven current are important.

Another consequence of the Ekman layer reaching to the bottom is that the damping of the wind response switches from being through internal stress to bottom stress. To include tidal and other barotropic currents in a quadratic estimate of the latter, we use the speed from a previously converged run of the model rather than the present to preserve the linearity of the model in terms of its control variables. For any implementation of quadratic stress, the speed fields of the forward integration must be stored for use in the adjoint model. We have reduced the storage requirements by only storing the current speed fields at intervals short enough to

resolve the tides (1.5 hours), then interpolating between retrieved values.

Cost Function

The cost function used here is identical in form to that described more completely by TG. It includes terms (see appendix) measuring the squared misfit of the model to the data and terms that penalize the volume transport and vorticity of the barotropic component and the current velocity of the geostrophic component. Data types available (described further in the next section) comprise bottom pressure at two points and currents measured by current meters, drifters, and a shipborne ADCP. Hindcasts (from harmonic analysis of the data) of the tidal current at the locations of the current meters are also assimilated at low weight for the few days before instrument deployment and after retrieval. The bottom pressure data constrain only the barotropic model, while the currents constrain the sum of the barotropic and geostrophic models. We explain in the appendix how the bottom pressure data are leveled by treating the means as control variables and how the pressure differences between sites are fit more closely than the individual pressures.

All terms of the cost function are normalized but the choice of the normalizing weights is not straightforward. We have elected to use an empirical approach and create an artificial data void of 15.8-km radius (shown as a dashed circle in Plate 1) in the model's domain so that the data from within that area can be used as an objective measure of the model's ability to interpolate dynamically between areas where data are supplied. The optimal choice of weights maximizes the model's interpolative skill (much like the optimal choice of control variables minimizes the cost function), but we do not search the entire multidimensional space of all the weights to find the truly optimal values. The most important ratio of weights is that between the data and penalty terms. If the data are fit too closely, the hindcast of the withheld data indeed turns out to be poorer. Hindcasts are also poor if the data are fit too loosely because the model current field is then too smooth and weak. In the following we only show results using the (approximately) optimal weights (with and then without the data void imposed).

Observations

The data acquisition systems, which are detailed by *Bowen et al.* [1995], included, briefly, the following: (1) two telemetering moorings, equipped with acoustic transponding InterOcean S4 current meters at 20 and 40 m, and Aanderaa WLR6 pressure gauges at the bottom (48 and 50 m, respectively, at the central and east moorings, see Figure 1); (2) two nontelemetering moorings (southeast and west), each carrying one S4 current meter at 20 m in 58 and 54 m of water, respectively; (3) 14 telemetering Loran C or Global Positioning System equipped drifters with 10 m × 2 m drogues centered at 20 m; (4) a 300-kHz RD Instruments acoustic Doppler current profiler mounted in the hull of the M/V *Petrel V*; (5) a masthead weather station; (6) a Seabird 25 CTD probe; (7) a pair of 0.28 m^2 bongo nets with 333-μm mesh; (8) a 1 m^2 EZNET (Eastern Marine Marsh, Dartmouth, Nova Scotia) version of the Bedford Institute of Oceanography Net and Environment Sampling System (BIONESS) [*Sameoto et al.*, 1980] fitted with 10 remotely closed 333-μm mesh nets, a Seabird 19 CTD, and an optical plankton counter; and (9) a network of 10 data aquisition personal computers and 7 Sun Microsystem SPARC 2, 1+, and SLC workstations for data analysis.

The current meters carried sensors for pressure, temperature, and salinity. The bottom-mounted pressure gauges also measured the temperature, as did the ADCP at keel depth (4 m). The temperature and salinity data are not assimilated into the model. The temperature data reveal much about the circulation of the bank, especially in conjunction with the model's velocity field as shown below.

We chose not to assimilate the two 40-m current meter records due to their proximity (8-10 m) to the bottom. The 20-m records are very similar to the 40-m records for subinertial frequency variability, so we also chose not to vertically average.

Processing of data from the moored and drifting instruments was straightforward (although for the real-time use of the data some preprocessing was required to catch transmission errors). The original samples (taken every 5 min for 2 min) from the current meters and pressure gauges were low-pass filtered (half power at 1.2 hours) and subsampled at 30-min intervals.

The current meter pressure data indicate that mooring line tension was sufficient to maintain instantaneous meter depths within 4 m, usually 2 m, of the minimum, despite strong currents during storms, so no corrections were made for tilt.

The drifter data, which comprised position fixes every 30 min, are discussed in detail by *Sanderson* [1995]. The original fixes were manually corrected for Loran C lane jumps then differenced to estimate velocities. The resolution of the fixes is such that the velocities estimated in this way are no noisier than the current meter data.

The bottom-track velocity used to Earth reference the ADCP data was carefully screened for false returns from gear deployed over the side. These were detected by comparing the bottom-track depth with the sounder depth. Numerous other quality control criteria were also imposed. For assimilation to the model we depth average the velocity profile between 10 m and 85% of the water depth and time average over 15 min.

Wind observations were made every 1 min at the masthead (10-m elevation), corrected for the ship's heading and speed, then averaged over 15 min. During two storms that forced the ship back to port, wind data, recorded hourly between 0500 and 2200 local time, from the Atmosphere Environment Service station at nearby Sable Island were used. The reported gust velocity

rather than the average velocity agreed more closely with our observations when there was overlap and hence was used to fill the gap in our record. Wind stress was estimated from velocity by the neutral steady state formula of *Large and Pond* [1981].

Description of Events

The first 3 days of the cruise were devoted to gathering CTD, Bongo net, and ADCP data on eastward, northward, and southwestward transects of Western Bank (see Plate 1), concentrating on the bank crest (denoted by the 40-m isobath) where previous work had shown tidal residual currents to be the weakest [TG] and larval abundances to be the highest [*O'Boyle et al.*, 1984; *Brander and Hurley*, 1992].

The waters sampled on the bank can be broadly categorized as warm, saline, slightly denser (10.4°C, 32.3 practical salinity units (psu), 24.6 kg m^{-3}) water (WSW); cold, fresh, slightly lighter (8.4°C, 31.2 psu, 24.4 kg m^{-3}) water (CFW); or intermediate (9.2°C, 31.6 psu, 24.5 kg m^{-3}) water (IW), which appears to be a mixture of CFW and WSW. The WSW (red in Plate 1) was initially found at several shallow stations near the crest of the bank or westward and northwestward, and also in deep water southward of the 80-m isobath (just off Plate 1); it is predominantly oceanic and flows onto the shelf between Western and Emerald Banks. The CFW (blue in Plate 1) was initially found from the surface to the bottom in the shallow water east of the crest and down to 30 m as far south of the crest as the 80-m isobath; it is presumably of Gulf of St Lawrence origin. The IW (green-yellow in Plate 1) separated the other two water masses either as a thin layer or as a large mass near the crest of the bank.

The wind from the ENE was strong enough to suspend steaming and biological sampling for a period covering panels labelled 1 and 2 of Plate 1, during which time the WSW water initially sampled near the crest of the bank was replaced by IW. This mass of IW was chosen for continued biological resampling because the larval abundances were indeed much higher than elsewhere (see *Taggart et al.* [1995] and below), and the tidal residual current, calculated by subtracting previously computed tidal current field predictions from the ADCP data, was very weak.

We cannot be sure where or when the bulk of the IW was formed, but the important observation for the purpose of the cruise is that IW rotated clockwise atop the crest of the bank from November 26, when drifters were deployed and intensive biological sampling started, to December 3, when the first leg of the cruise was terminated by the onset of storm-force winds. During this time the IW was bounded to the east, south, and eventually also the west by a tongue of CFW flowing clockwise around the crest of the bank. *S. E. Lochmann et al.* (Abundance and condition of larval cod (Gadus morhua) at a convergent front on the Eastern Scotian Shelf, submitted to *Canadian Journal of Fisheries and Aquatic Sciences*, 1995) discuss the biological implications of the front between the IW and CFW, which was

convergent enough to draw several of the drifters into a line by 1645 UT on November 28 (see panels labelled 5 and 6 of Plate 1). Hence the IW over the bank crest was largely surrounded by lighter water, so a local picture of an anticyclonic eddy is not a sufficient description. The anticyclonic sense of rotation can only be explained in a larger picture that includes the WSW.

The rotation of the IW is clearly depicted by the drifters, particularly drifter 8, which completes a full circuit around the other drifters and the crest of the bank (panels labelled 4–10). Drifters 6 and 13, which were deployed at the northeast extreme of the cluster, behaved very differently: both were lost from the IW into CFW at about the same time and place (see panels labelled 5 and 6 of Plate 1). Drifter 6 moved very rapidly to the west (panels labelled 8 and 9 of Plate 1), but drifter 13 remained close to the east current meter (where the 25-hour-mean current was so small that the arrow does not show) until the onset of the storms. The 11 other drifters separated off singly or in pairs, except for drifters 12, 16, 18, and 20, which remained together in IW throughout the experiment.

Strong easterly winds blew on December 3, changing to strong westerlies on December 4 and 6. The drifters all went briefly to the northwest, then quickly south. The second leg of the cruise commenced on December 7, and seven drifters were immediately retrieved, some from beyond the 200-m isobath. They were redeployed in a small cluster near the group of drifters that remained within what seemed to be the only intact parcel of IW. Biological sampling was concentrated in that small parcel after a 2-day, broader scale survey found no other water with both (1) the temperature (reduced by ~ 1° by cold winds) and salinity of IW and (2) appreciable numbers of cod larvae. A sustained northwestward flow during leg 2 swept all drifters landward off the bank, biological sampling ceased, and the drifters were retrieved on December 14. Water temperatures over the bank fell throughout December, but salinity (not shown) was constant or increased. The moorings were retrieved on December 15.

Fit of the Model to Data

For the model run discussed in this section, only data recorded more than 15.8 km from the central mooring are assimilated so that the model's skill at hindcasting the current at the central mooring can be assessed. The east mooring is just outside this exclusion zone, but many drifters and the ship were often within it, as shown in Plate 1.

Convergence of the descent method is illustrated in Figure 2. Note that some terms of the cost function are numerically much greater than others, so it is essential that convergence criteria be imposed on all terms. The term of the cost function measuring the squared misfit of the model to the currents is the greatest and reduces quickly at first so that by iteration 3, 76% of the observed velocity variance is reproduced by the model. By iteration 40 this figure is 92.8% and another 460 iterations only increases it to 93.3%, while increasing
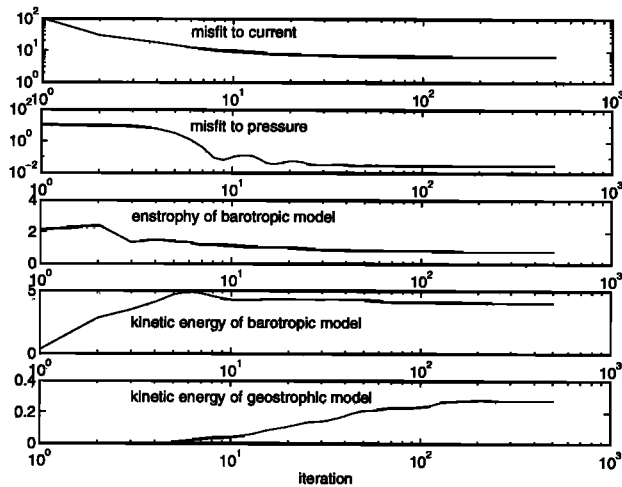
Figure 2. Magnitude of the terms of the cost function as a function of iteration number.

the mean squared velocity of the geostrophic component of the model by 50%. The slow convergence to stable values of the control variables for the geostrophic component is clearly a key problem with the model. Convergence is much faster if the mean squared geostrophic velocity is penalized more heavily, leading to less of the observed variance being explained by the geostrophic model, but then the interpolative skill of the total model suffers. The root of the problem is that the barotropic and geostrophic model components are almost equally capable of accounting for a portion of the observed current variability. Other data types [see TG] are needed for a cleaner separation.

Pressure at only one site is assimilated for this example (the other site is in the data void), so 99% of the variance can be reproduced by the model. Results of assimilating the data from the second pressure gauge need not be discussed here. A separate deployment of four pressure gauges on Western Bank provides a more interesting study and will be discussed elsewhere.

Time series of the model's fit to the observations are shown in Figure 3. The model errors are clearly small (as evident in Figure 2), indicating that the model has enough degrees of freedom, even with only two control variables per boundary and an order 4 polynomial for the geostrophic pressure field.

Importantly, the model hindcast errors of the withheld data are not much greater than the misfits to the assimilated data, indicating that the model is not overfitting the assimilated data. The withheld data shown in Figure 3 include those from drifter 8 for almost the entire period from deployment to December 4, about half of the ADCP data during that period, the other three drifters for the initial 24 hours and, of course, the central meter for the whole deployment. The model errors for drifter 8 are comparable with those of the other drifters, while the main contributor to the total error at the central meter is a model bias of 0.08 m s^{-1} southward from December 3 onward.

The spatial structure of the subtidal component of

the model's flow field and of the current meter data is shown in Figure 4. The 25-hour-mean fields clearly have complicated structure, particularly panels labelled 6 to 9 in Figure 4, which cover a wind-free period and show an eastward current swinging to southward at the central mooring in excellent agreement with the (withheld) observations there. The response to the minor storm of November 27 (panel 5) and the major storms of December 3–6 (panels labelled 10–13) is more uniform but still includes considerable velocity differences at the current meter sites, structure that is reproduced by the model.

The contributions to the total flow field by the geostrophic and barotropic components of the model are shown in Figures 5 and 6, respectively. They show it is the geostrophic component of the model that reproduces the mean trajectory of the eddy in the center of the model's domain, leaving the barotropic model to explain the tides (see Figure 3 and TG) and storm response for which it is better suited. The polynomial description of the eddy is acceptable for interpolation and extrapolation over short distances but inevitably results in unrealistic flows well away from the data (see, for example, the northeast corner of the model's domain).

Comparison With Alternative Hindcasts

The model is clearly good at hindcasting the current at the central mooring using observations outside the data void. Could this have been achieved with a simpler scheme? The simplest scheme is to assume the current at the central mooring is equal to the nearest observation outside the data void. The radius of the void is such that the east mooring always provides the nearest observation. The west mooring is the next closest mooring, but drifters or the ADCP are generally closer, so a weighted average of all the observations is a reasonable improvement on using only the nearest. We have weighted the observations by distance^{-3} for an alternative hindcast.

The skills of four hindcasts of the central mooring current are compared in Figure 7. Only the clockwise component of the rotary spectral analysis is shown because the energy density of the anticlockwise component is much less. The assimilation model clearly gives the best hindcast; the coherence is high for all energetic spectral components, the gain is unity, and the phase near zero. The weighted average is next best but has gain and phase errors for the diurnal tide and poorer performance for the 2-day-period spectral peak. Similar errors arise when the nearest (east) meter is used alone.

Coherence of the current at the central mooring with the wind stress is also shown in Figure 7 to demonstrate how poorly even the best linear model driven only by the wind can perform as a hindcast of the current. The coherence is almost as high as achieved using the model, but only for the 2-day-period spectral peak of the wind. Hence a wind-driven model can do nearly as well as the assimilation model for the storm response, but only if it correctly accounts for the observed gain and phase,
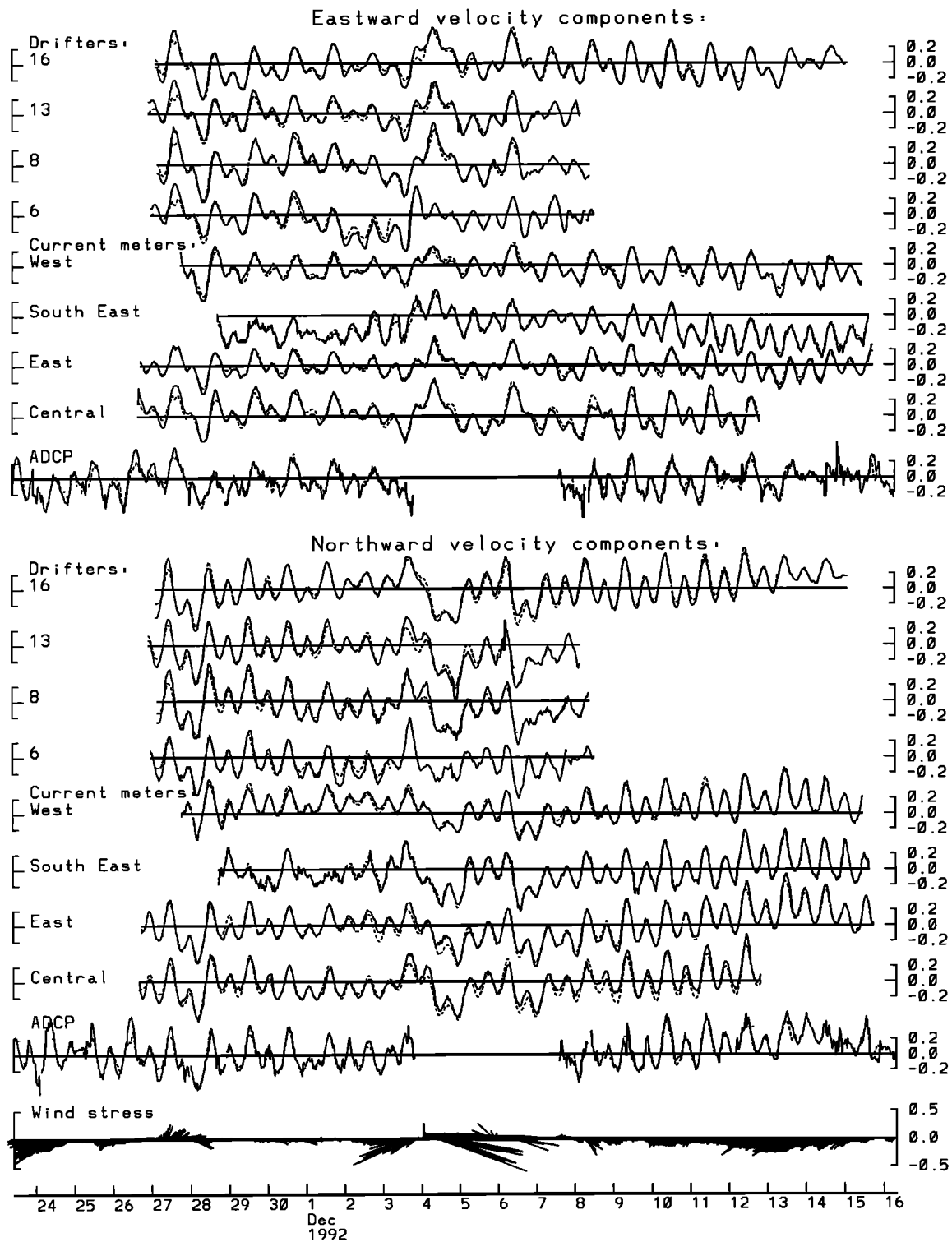
Figure 3. Model fit (dashed lines) to the velocity (meters per second) observed from drifters, current meters and the acoustic Doppler current profiler. Only four representative examples of the 14 drifter time series are shown. Data from inside the dashed circles in Plate 1 are not assimilated. Wind stress vectors (newtons per sqaure meter) show generally NE winds, except for the storm force wind from the WNW.
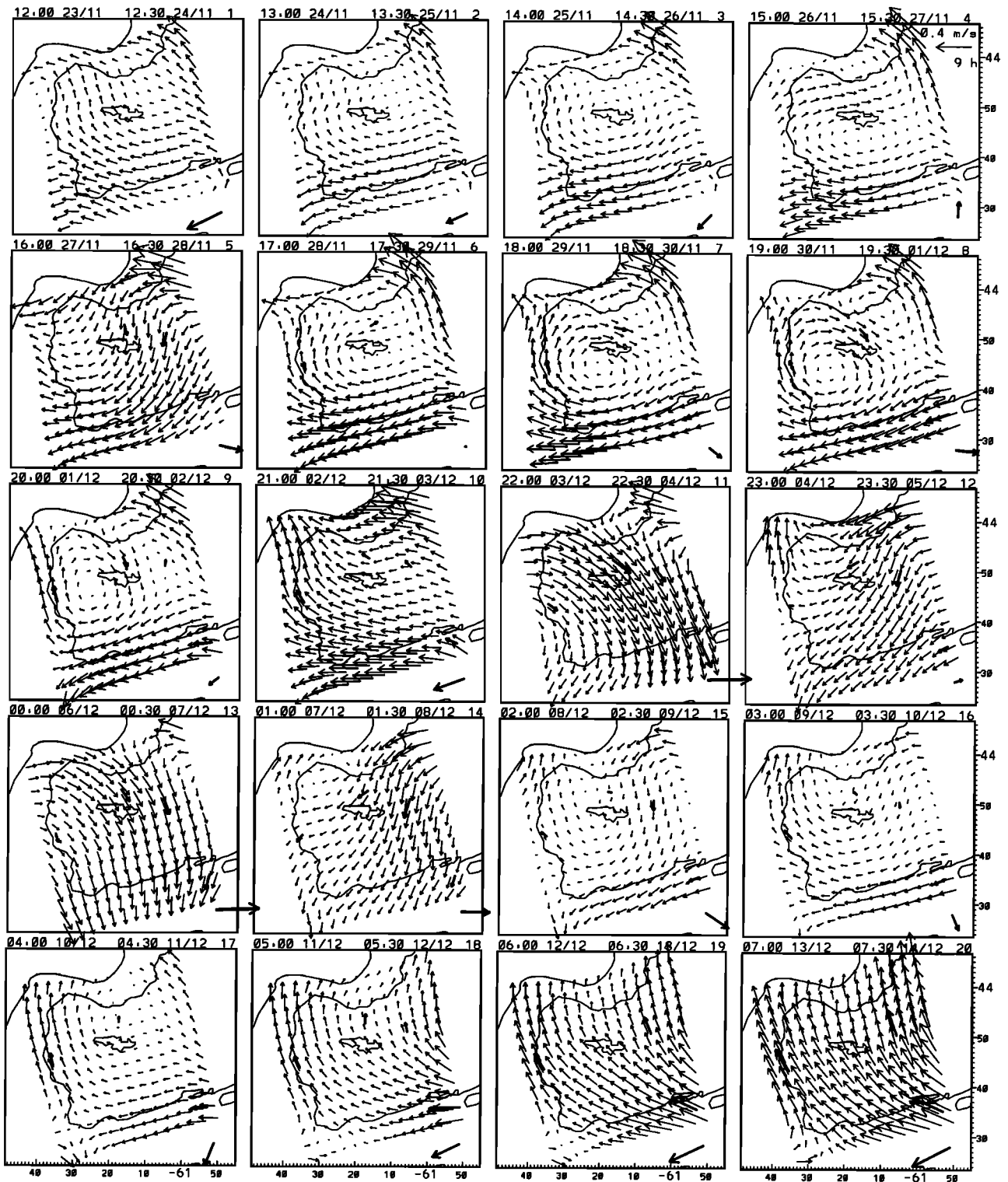
Figure 4. Sequence of 25-hour-means of the model's flow field, the current meter observations (bold arrows) and wind velocity observations (bottom right of each panel, reduced to 3%). Data from inside the dashed circles in Plate 1 are not assimilated.

which are quite different at the different moorings. The appreciable difference in the amplitude of the wind response at the four moorings is the reason the slab model used by TG was not adequate for modeling the wind response for the data set discussed here.

The present application called for tracking a water mass so the importance of spectral components of the velocity reduces as frequency increases. The most direct assessment of the accuracy of such tracking might seem to be the success with which schemes hindcast the
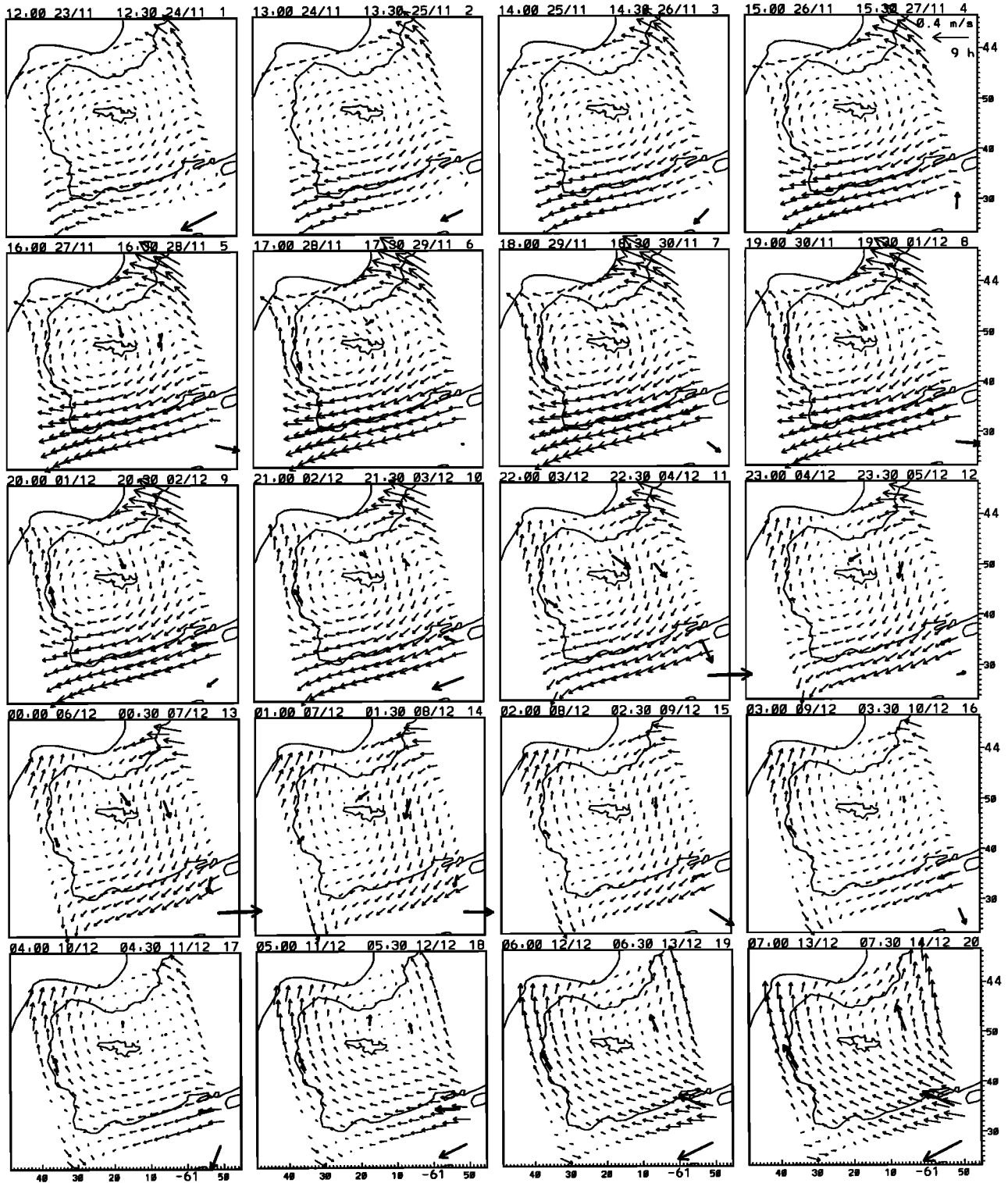
Figure 5. Same as Figure 4 but showing only the geostrophic component of the model's flow field.

trajectories of real drifters. However, the nonlinearity of the Euler-Lagrange transformation amplifies small model and observational errors at critical places, a hyperbolic point of the flow, for example. We prefer to compare the various schemes' abilities to hindcast the integral of the velocity at the central mooring (Figure

8). Of the twelve 25-hour periods shown, there is only one (panel 6) during which the weighted average of the surrounding data is a better hindcast than the model's. The superiority of the model hindcast is most evident in panel 5, where the modeled velocity integrates to about 8 km southeast, in good agreement with the central
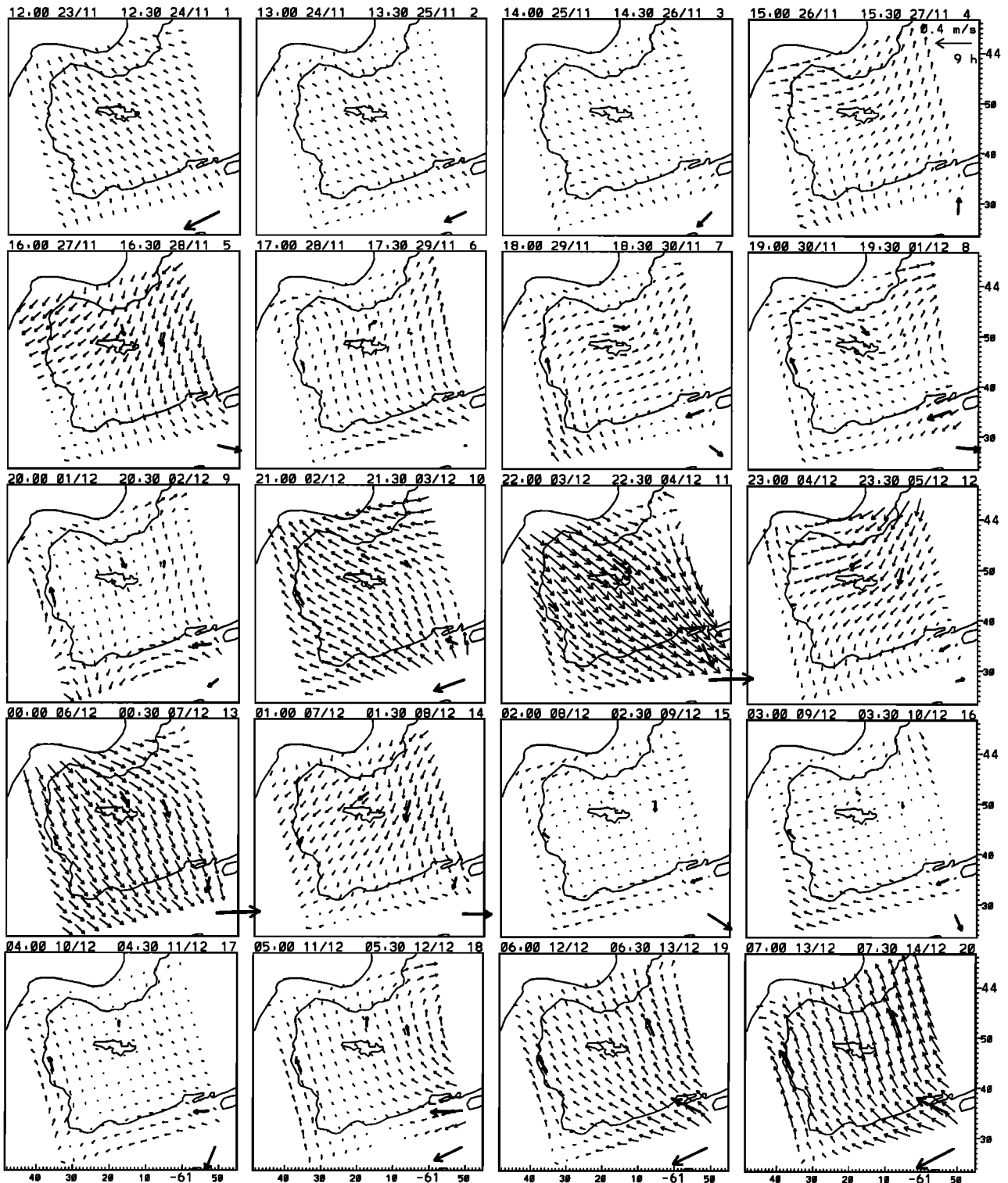
Figure 6. Same as Figure 4 but showing only the barotropic component of the model's flow field.

mooring current, while the average of the surrounding observations integrates to 7.5 km northwest, an error of 200%. Figure 8 also shows the model's hindcast of the current at the east meter for comparison with the data to demonstrate that its errors are not significantly less where data are used (east) than where they are not (central), at least in the central region of the model's domain.

Use of the Flow Field

In this section we show how a model of the flow field can be used to advantage during and after oceanographic fieldwork. Only hindcast runs assimilating all available data are used because these adequately illustrate what was achieved in real time. The differences are minor where it mattered for operational purposes, so
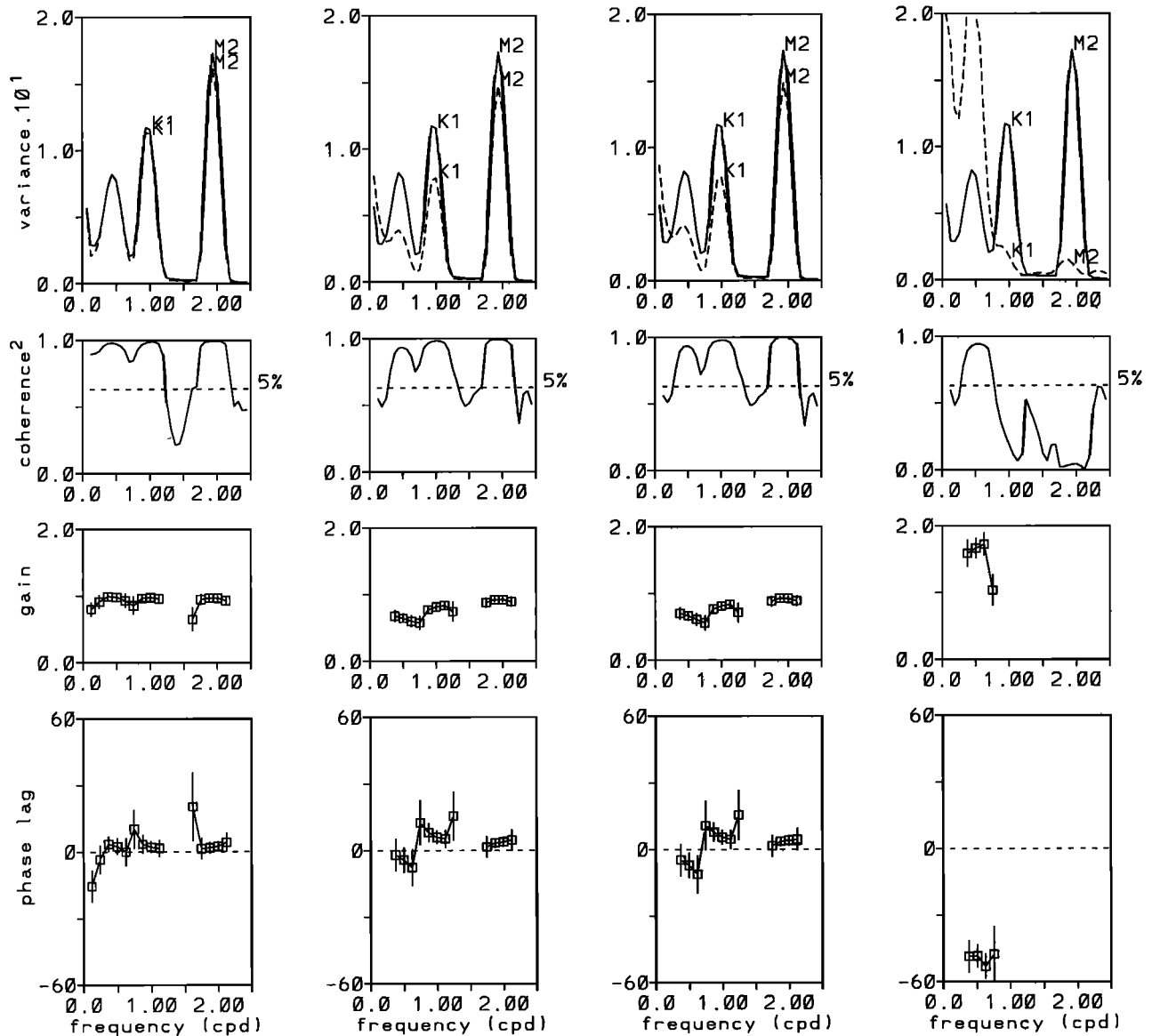
Figure 7. Rotary cospectral analysis of the observed central mooring current with four other time series (from left to right): central mooring model hindcast, assimilating only data farther than 15.8 km from the central mooring; distance^{-3} weighted average of all velocities assimilated to the model; velocity recorded at the east meter (15.9 km away); and the local wind stress. The top row of panels shows the spectra of the clockwise rotating components of the central mooring current (solid lines) and the other time series (dashed lines). Tidal peaks are labeled. Subsequent rows show, respectively, the clockwise rotary coherence between the central mooring current and the four other time series; the gain (other/central); and the phase lag of the other time series behind the central mooring current. The analysis period is 16.1 days from 1800 UT on November 26, 1992. The linear frequency axis is cycles per day (cpd), and the linear variance axis has units of $(m\ s^{-1})^2/cpd$ or $(N\ m^{-2})^2/cpd$, so the spectra are energy-preserving. Cross-spectral phase estimates are separated by half the width at half amplitude (four harmonics) of Tukey window frequency domain smoothing, so every second point is independent.

there is little point in recreating the data availability at sea. Naturally, no data are withheld from assimilation (unlike in the preceding section).

As discussed in the Observations section, the first 3 days of the cruise were spent surveying the bank to choose the best location to start the tracking experiment. We hoped to find an isolated concentration of cod larvae. However, by the time such a ship survey

is finished, the waters sampled in the early stages have quite likely moved considerably and may be difficult to relocate for resampling. To ameliorate this problem, we used the model's flow field to keep track of all waters sampled so that data acquired during the course of the survey could be displayed as if they were acquired synoptically.

The success of this approach obviously depends on
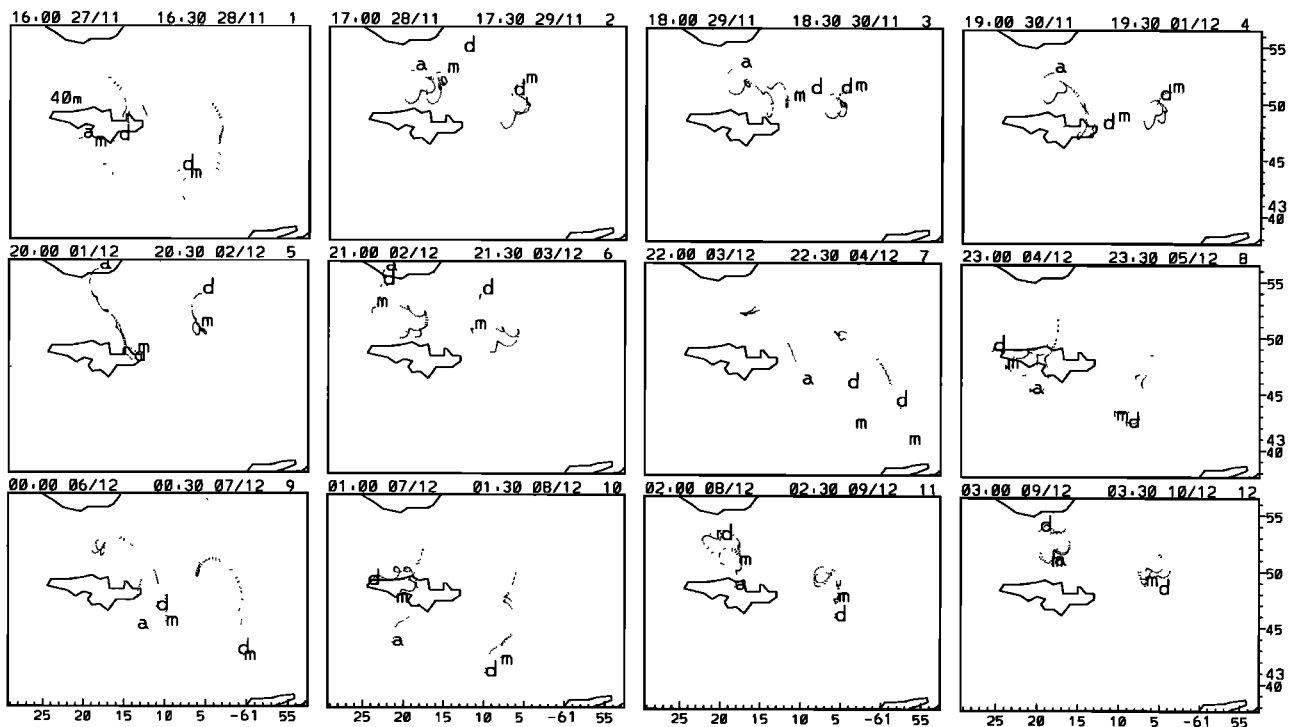
Figure 8. Comparison of the assimilation model's ability to hindcast integrated current velocity with that of a simpler scheme. Each panel spans 25 hours and shows progressive vector diagrams (PVDs) of five velocity time series. Three originate at the site of the central current meter north of the bank crest (closed 40-m isobath) as follows: one for the data there (labelled d); one for the model's hindcast (labelled m) at the central mooring assimilating only data farther than 15.8 km from the central mooring, and one for the distance^{-3} weighted average (labelled a) of all assimilated velocities. The remaining PVDs originate from the east site (15.9 km from the central mooring) and are of the data (d) and the model's hindcast (m) there.

the accuracy of the model and the degree to which the measured quantities are advected passively and conservatively. Let us assume that over a period of a few days both the density of cod larvae and the water temperature are advected passively and conservatively without diffusion according to the model's flow field. Although simplistic, these assumptions should be an improvement over the usual assumption that the velocity field is zero, or at least locally parallel with isolines of the measured quantities.

The survey was limited to an eastward transect of the bank followed by northward and southwestward transects, each crossing the eastward transect near the bank crest. At both intersections the sea surface temperature (SST) was ∼1C° lower at second sampling (Plate 1 and 2), so the water was clearly not stationary or just flowing along isotherms. Plate 2 (bottom) shows that, according to the model, the water sampled during the eastward transect shifted westward by about 8 km before the second and third transects were completed. This shift completely explains the observed cooling because of the spatial temperature gradients, so since the temperature data were not used by the model, this is independent evidence that the model's

flow field is correct (assuming the water temperature was approximately conserved and advected passively).

The density of cod larvae found during the survey is also shown in Plate 2. By the end of the three transects, appreciable larval densities had been found only in IW, both at the north of the survey area and during the second pass over the crest of the bank. The bank crest was chosen for continued sampling in preference to the northern area because the tidal residual current was weaker at the crest, and previous cruises to the area had consistently found greater larval abundances and weakest tidal residual currents over the bank crest. The third visit to the crest found IW still there, in agreement with the model running in real time, and the density of larvae was high, so the drifters were deployed and sampling with the EZNET began.

We cannot be sure what would have happened had we chosen the northern area because we did not make many more current observations there. We can, however, be sure that if the cod larvae had been found in the CFW east or south of the crest, any patch of CFW water consequently chosen to sample would have been torn apart much quicker than was the patch of IW actually chosen. This can be seen in Plate 3, which shows the simulated

evolution of the SST field during the study period. The first panel depicts WSW offshore and wrapped anticyclonically around some IW over the crest of the bank. The nine following panels show CFW sweeping from the east around the IW over the crest, replacing the WSW (at least in the surface layer). Then the storms hit and bank waters move briefly landward, then ~ 40 km seaward. They subsequently flow landward off the bank, being replaced by water predominantly from the east. Unfortunately, no satellite images of SST are available to validate the sequence because cloud cover was complete for the whole cruise.

To produce the simulation, the ship's SST observations are advected both forward and backward for up to 75 h using the model's flow field. Coverage is further extended by advecting 3-hourly temperature observations made by the four current meters 20 m from the surface, also for up to 75 hours forward and backward. Thus each observation appears in Plate 3 in the three panels before and the three panels after it is made, each time at the location where the water is hindcast to have been. The simulation is remarkably self-consistent in that observations are essentially spatially sorted by temperature, even if the times and places of the observations differ by up to 150 hours and tens of kilometers. Most interestingly, a linear thermal front between IW and CFW is hindcast to have been close to the line to which several of the drifters converged. The model therefore seems to be realistic enough for our purposes, despite its relative simplicity compared with reality.

Summary and Discussion

We have developed a shelf circulation model with data assimilation to the point that it could be used as an operational tool at sea during a 21-day cruise on the Scotian Shelf. The data assimilation enables the model to reproduce 93% of the observed current variance, while still having interpolative skill. The model does not, of course, have predictive skill outside the period of our observations (except for a short term forecast based on its final-state), but that is not its purpose.

The model, particle tracking, and graphics software worked well as a synthesizer, for cruise planning purposes, of the velocity, temperature and larval density data. The system contributed substantially to the successful outcome of the cruise primarily by assisting us to keep track of all the waters sampled. A weighted-average method of interpolating the velocity field from scattered observations could have been used and indeed was used operationally with the other software during the earlier April 1992 pilot cruise to the bank, but it is clear that simple methods of interpolation cannot match the interpolation skill of our model with data assimilation. We hope to have demonstrated that such models are feasible and worth the extra effort and cost.

The process of designing a model with data assimilation by the adjoint method comprises (1) design of the observation network (unless it is predetermined); (2) choice of the model to be fit to the data; (3) choice of its control variables, i.e. deciding which model parameters and independent variables to infer by assimilation, and how they might be reparameterized; (4) design of the cost function; and (5) choice of a gradient descent algorithm. The power of a variational data assimilation scheme is that model parameters and independent variables whose values are not known can be inferred from observations of the dependent variables; but an ocean model usually has many more unknowns than there are observations. One way to reduce this null space is to reduce the number of unknowns by reparameterisation [Chavent et al., 1975] and another is to augment the cost function with penalty terms [Thacker, 1988], so steps (3) and (4) are linked. We found that expressing the flows through the four open boundaries of our model's domain in terms of a small number of orthogonal polynomials was better than penalising spatial variability of the flow and that interpolating timewise from boundary flows defined only every 1.5 h was better than penalising high frequency variability. (By better we mean here that many less iterations were required to find the minimum of the cost function.) While costly, the technique of penalization is still attractive due to its greater flexibility and we find it essential to penalize the volume transport and vorticity of the entire flow field.

For the model runs presented here we set the initial conditions to zero long enough before the first observation is assimilated for the early boundary fluxes to spin up the quiescent interior. However, some states of a barotropic ocean cannot be reproduced in our barotropic model this way because the model has no advection of momentum. For example, an eddy over closed isobaths can only be reproduced by also treating the initial conditions as control variables. Just such a feature occurs in our observations, but it is clearly also associated with the density field. So rather than attempting to model the eddy's temporal evolution dynamically, we allow the low-frequency, essentially geostrophic component of the observed current to be described in a second component of the model by a time series of coefficients for a polynomial expansion of the geostrophic pressure field at 20 m (demonstrating how steps (2) and (3) are also linked). With the eddy thus accounted for the barotropic model is capable of fitting the remaining observed currents if forced only at the boundaries, obviating the need to infer the initial conditions and also, to some degree, the need to include advection of momentum. The latter is a significant saving because Gentry et al.'s [1966] second upwind (donor cell) method of advecting momentum, activated only during the final integration of the forward model, proved too viscous for our application, and to fully implement this nonlinearity would require not only another layer of control variables along each boundary and a more complex adjoint model, but also a solution (see Vogeler and Schröter [1995] for an innovative approach) to the technical question of how to find the absolute minimum of a cost function with potentially many local

minima.

We chose not to infer C_D by data assimilation but set it to a constant and used values of v^* from a converged model run to estimate a quadratic bottom stress. One advantage of this approach is that the problem remains linear in terms of the control variables and so a very efficient minimisation algorithm [see TG] can be used. The model hindcast is not as sensitive to changes in C_D as a model without assimilation because the assimilation scheme can partially compensate for changes in C_D by changes in the boundary flows. We chose a value of C_D the same way we chose the ratio of weights in the cost function, by maximising the interpolative skill of the model in an artificial data void.

A minor data source for the present work was the two pressure gauges. Two problems are associate with assimilation of pressure data to a model such as ours. One is how to level the gauges. We did this by defining extra control variables for each gauge so that dynamic pressure offsets of the record means (slowly time-dependent, due to calibration drift) could be inferred from the velocity data dynamically by the model. The second problem is that the absolute pressure of the model is sensitive to small departures from nondivergence through the continuity equation. Hence an attempt to fit the absolute pressures leads to ill-conditioning of the problem if many boundary flux control variables influence the net divergence. We improved the conditioning by expanding the boundary fluxes in terms of structure functions chosen such that only the first controlled the mean. Conditioning was still poor if the absolute pressures were fit closely enough for the observed pressure gradients to be reproduced, so we fit the absolute pressures with a large tolerance and differences across the array with a small tolerance. These measures allowed all the dynamically important information to be extracted from the data, without significantly slowing convergence of the assimilation scheme.

The dominant source of data for the present model was the 14 drifters of *Sanderson* [1995]. We differentiated the trajectories, assimilated the velocities, then integrated the model velocities in order to track our target water mass. Why not track that water mass by just following the drifter centroid or, if committed to using an Eulerian numerical model, assimilate the drifter trajectories themselves? Had the flow over Western Bank been more uniform than it was, either approach might have worked; but, in fact, the complex gyral circulation and presence of the front between water masses, combined with the small imperfections of the drifters as Lagrangian particles, conspired to render the drifter trajectories too complex for either approach. We took an approach that was more likely to succeed and which did not depend solely on the drifters. We could probably assimilate the drifter trajectories themselves if we used only a subset of them or treated them as many short subtrajectories following *Kamarchi and O'Brien* [1995]. The duration of each subtrajectory is then an important parameter which we have effectively set to 30 min, while Kamarchi and O'Brien chose 1 day.

For the first few days of our cruise the only current data available to the model were from the ADCP. To model the tidal-residual current in real time using only the ADCP data we (1) detided the current by subtracting predictions of a tidal model run for the cruise period and calibrated using data from earlier cruises, then (2) assimilated the tidal residuals to the model with the time step of the control variables increased to 12 hours and the model grid enlarged so that the ship was within it for more of the time. The resulting flow fields were quite similar to the hindcasts of the early days produced using data from the whole cruise. An alternative approach that we would like to explore is to make spectral expansions in the time domain of the boundary fluxes. The subtidal variability could then be allowed to have smaller spatial scales than the tidal component, and prior knowledge of the tidal constituents could be more easily incorporated. It may also be fruitful to penalize departures from a typical ocean current frequency and/or wavenumber spectrum rather than simply the volume transport and vorticity, as we have done here.

The present paper has focused on the feasibility and attractiveness of a shelf circulation model with data assimilation rather than on the physical oceanography of Western Bank. TG summarize what was learned about the circulation of the bank from two spring cruises. From the winter cruise discussed here we learned more about the role of physical influences in the survival of cod larvae. The eddy observed over the crest of the bank during the first leg of the cruise clearly provided a more stable environment for larvae than the surrounding waters, perhaps explaining why larval densities have repeatedly been observed [*O'Boyle et al.*, 1984; *Brander and Hurley*, 1992] to be relatively high there. However, that was only the case until the onset of the storms, which generated waves up to 14-m high at the Sable Island oil platform and drove most of the bank waters seaward close to the shelf break. Sustained easterly winds after the storms contributed to the northwestward flow observed during the final leg of the cruise, but the current speeds were much greater than can be explained by the measured wind. Hence we cannot yet predict or hindcast with confidence how often the bank waters are replaced during the spawning period, but we can say that there are periods when larvae will enjoy stable conditions for a month or more, at least over the bank crest. It therefore seems quite plausible that large fluctuations in larval mortality are associated with the variable integrity of the eddy.
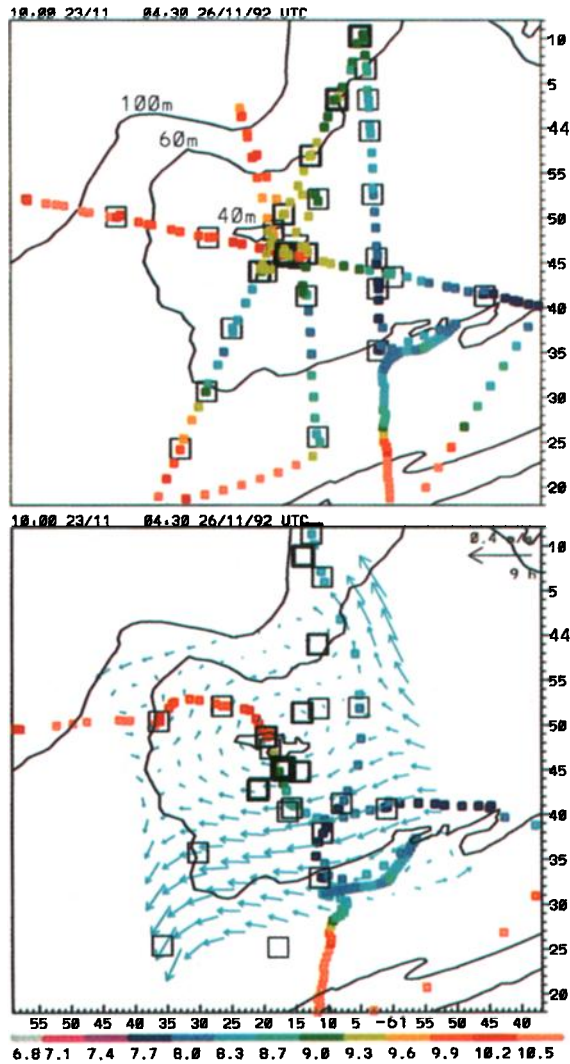
Appendix: Details of the Assimilation Scheme

The purpose of this appendix is to document technical details of the model, its control variables, the cost function, and then how the gradient of the cost function with respect to the control variables is calculated.

Basic Model and Control Variables

First, we define the dimensionless variables and parameters

10.00 23/11   04.30 26/11/92 UTC

10.00 23/11   04.30 26/11/92 UTC

55 50 45 40 35 30 25 20 15 10 5 −01 55 50 45 40
6.8 7.1 7.4 7.7 8.0 8.3 8.7 9.0 9.3 9.6 9.9 10.2 10.5

Plate 2. Sea surface temperatures (SST) and densities of cod larvae (top) where measured, and (bottom) where advection by the model's flow field places them at the end of the initial 2.8-day survey of the bank. SST is coded by the scale shown, while the line width of open squares is proportional to the density of cod larvae, which ranges from 0 to $1.4\,\mathrm{m^{-3}}$. Arrows indicate the average velocity from the model over the period.

$$x = x'/X \quad y = y'/X \quad t = |f|t'$$

$$u = u'/U \quad v = v'/U \quad p = \frac{p'}{\rho|f|XU} \quad h = h'/H$$

$$c^2 = \frac{gH}{|f|^2X^2} \quad C_D = \frac{C_D'U}{|f|H} \quad \tau = \frac{\tau'}{\rho|f|HU} \quad \text{(A1)}$$

in terms of their dimensional counterparts introduced in the text and here denoted by primes. X is the side of the (square) domain, U is a velocity scale, and H is the maximum depth (95 m). Dimensionless forms of (4)-(6) are then

$$\frac{\partial u}{\partial t} - \frac{v}{F} + \frac{\partial p}{\partial x} + \frac{(C_D v^* u - \tau^x)}{h} = 0 \quad \text{(A2)}$$

$$\frac{\partial v}{\partial t} + \frac{u}{F} + \frac{\partial p}{\partial y} + \frac{(C_D v^* v - \tau^y)}{h} = 0 \quad \text{(A3)}$$

$$\frac{\partial p}{\partial t} + c^2\left(\frac{\partial hu}{\partial x} + \frac{\partial hv}{\partial y}\right) = 0 \quad \text{(A4)}$$

where $F = |f|/f$. The flux at the (left, for example) boundary of the grid at time t (see (7)) is

$$h_{i,1}u_{i,1}^t = \sum_{s=1}^{S}\sum_{T=T1}^{T4} l_s^T\kappa(t-T)\chi_{s,i} - h_{i,1}\frac{p_{i,1}^t\cos\theta}{c\sqrt{h_{i,1}}} \quad \text{(A5)}$$

where l are control variables for the barotropic model. Here and in the following we use the convention that the first of two subscripts on a model field increases with $-y$, while the second increases with x.

The geostrophic component of the model is defined in continuous space and time, and the current components are given explicitly in terms of the control variables α (see (1)-(3)) by

$$(\dot{u}^t, \dot{v}^t) = F\sum_{s=1}^{S_d}\sum_{T=T1}^{T2}\alpha_s^T\omega(t-T)\left(-\frac{\partial\phi_s}{\partial y}, \frac{\partial\phi_s}{\partial x}\right). \quad \text{(A6)}$$

We will use subscripts below on $\dot{u}$, $\dot{v}$, $\partial\phi_s/\partial y$ and $\partial\phi_s/\partial x$ to denote the location at which these are evaluated, hence the use of overdots here rather than subscript d, as in the text, to identify this model component.

To distinguish the observations from model estimates, we will use the convention that observed quantities carry a tilde. A single subscript will be used both for observations and for model fields evaluated at the locations x_k^t of the observations. The subscript counts through all the observations of that type at that time. We use bilinear interpolation (denoted by the β weight function) between the four nearest grid points $x_{i,j}$ of the three barotropic model fields to evaluate model counterparts

$$p_k^t = \bar{p}_k + \sum_{i,j}\beta(x_k^t - x_{i,j})p_{i,j}^t \quad \text{(A7)}$$

$$(u,v)_k^t = \sum_{i,j}\beta(x_k^t - x_{i,j})(u,v)_{i,j}^t + (\dot{u},\dot{v})_k^t \quad \text{(A8)}$$

of the data. Note the inclusion of the geostrophic model component for comparison with velocity observations (all at 20 m), but not for bottom pressure observations. The unknown mean dynamic pressure perturbation $\bar{p}_k$ at each gauge is treated as a control variable of the data assimilation. Calibration drift is common with bottom pressure gauges, and this can also be inferred by allowing $\bar{p}_k$ to vary slowly with time (like the coefficients of the dynamic height field).

Cost Function and Lagrangian

The cost function

$$J = \sum_{t=1}^{N}\left[\sum_{k=1}^{n_p^t}\frac{(\tilde{p}_k^t - p_k^t)^2}{2\sigma_p^2}\right.$$
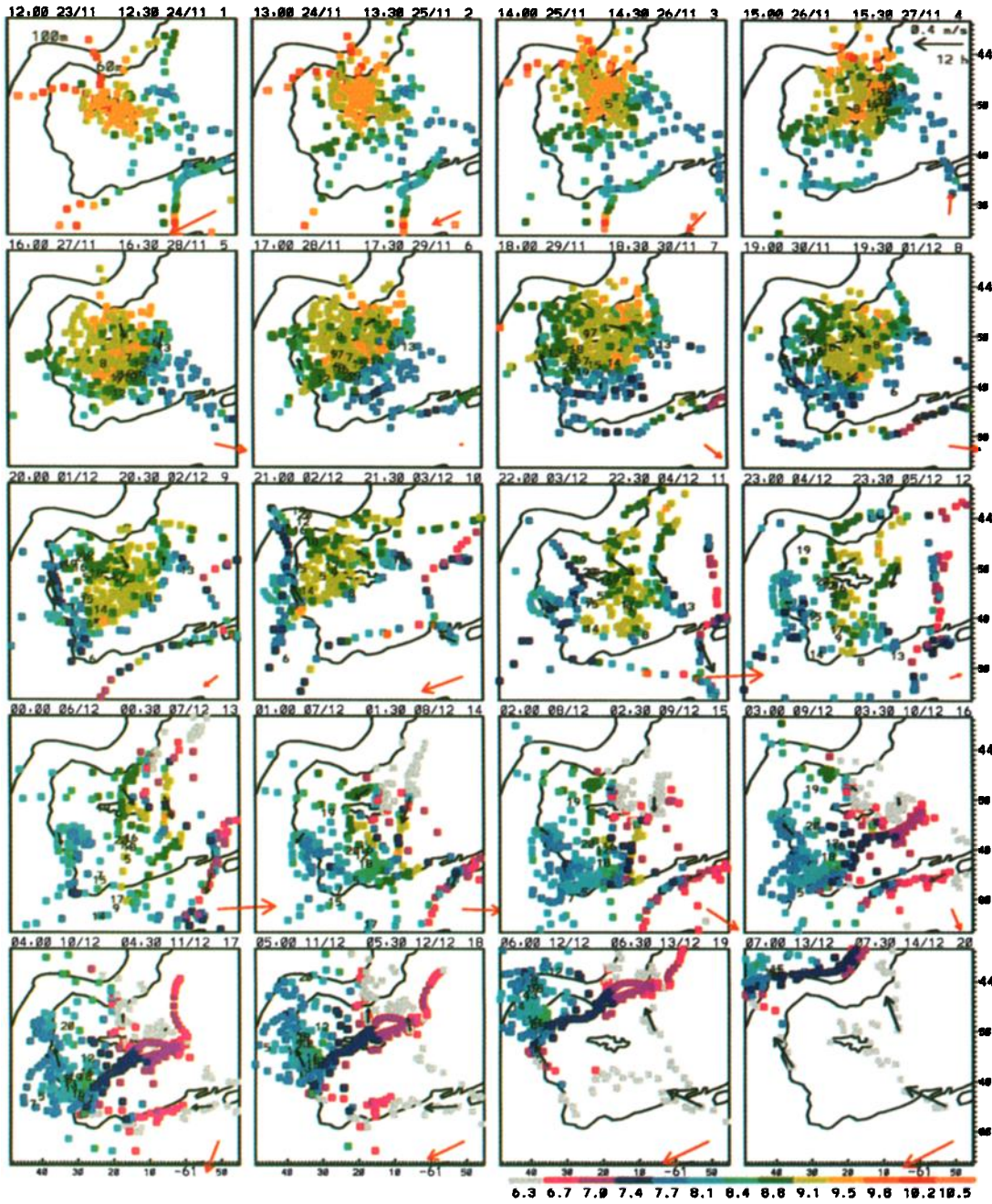
Plate 3. Evolution of the sea surface temperature field computed using the model's flow field. Panels show the positions every 25 hours of waters sampled by the ship and current meters during the preceding and succeeding 75 hours, color-coded by the temperature at sample time. Also shown are the drifter positions and 25-hour-mean observed currents and wind (see Plate 1).

$$+ \sum_{k=2}^{n_p^t} \frac{[(\tilde{p}_k^t - \tilde{p}_1^t) - (p_k^t - p_1^t)]^2}{2\sigma_{\Delta p}^2}$$

$$+ \sum_{k=1}^{n_u^t} \sum_{l=1}^{n_u^t} \frac{\psi_{k,l}^t}{2} \left[(\tilde{u}_k^t - u_k^t)(\tilde{u}_l^t - u_l^t) \right.$$

$$\left. + (\tilde{v}_k^t - v_k^t)(\tilde{v}_l^t - v_l^t) \right]$$

$$+ \sum_{t=1,\Delta T}^{N} \left[\sum_{i=1}^{n-1} \sum_{j=1}^{m-1} \frac{\zeta_{i,j}^{t2}}{2\sigma_\zeta^2} + \sum_{i=1}^{n} \sum_{j=1}^{m+1} \frac{(h_{i,j} u_{i,j}^t)^2}{2\sigma_v^2} \right.$$

$$\left. + \sum_{i=1}^{n+1} \sum_{j=1}^{m} \frac{(h_{i,j} v_{i,j}^t)^2}{2\sigma_v^2} \right]$$

$$+ \sum_{t=1,\Delta T_d}^{N} \sum_{i=1}^{n} \sum_{j=1}^{m} \frac{\dot{v}_{i,j}^{t2} + \dot{u}_{i,j}^{t2}}{2\sigma_u^2} + \sum_{k=1}^{n_p} \frac{\bar{p}_k^2}{2\sigma_{\bar{p}}^2} \quad (A9)$$

is a quadratic function of all the quantities that we wish to minimize, primarily the misfit of the model to the data. All terms of J are normalized, and TG discuss how we chose the weights. For the terms that measure the misfit to the data, the appropriate weighting is given by the inverse covariance matrix of the model errors. However, for the n_p^t pressure observations at time t we assume no covariance of errors and simply put σ_p^{-2} down the diagonal for the fit to absolute bottom pressures. We find it essential to have σ_p fairly large for the descent algorithm to work (see Discussion section) so this term functions mainly to reproduce the $\sim$ 1-dbar tidal pressure changes due to small departures from nondivergence. The smaller ($\sim$ 0.1-dbar) pressure differences across the array are fit by the next term with $\sigma_{\Delta p}^{-2}$ down the diagonal. For the n_u^t velocity observations at time t we estimate an idealized error covariance matrix based on instrument pair separations r at time t [see TG] with inverse ψ^t and elements

$$\sigma_u^2 = \sigma_v^2 = \left\{ \begin{array}{ll} \sigma_n^2 + \sigma^2 & r = 0 \\ \sigma^2 \exp(-r^2/2L^2) & r > 0 \end{array} \right.$$

$$\sigma_{uv} = \sigma_{vu} = 0 \qquad (A10)$$

where L is an error decorrelation length scale (we use 3.5 km) and the signal to noise ratio $\sigma/\sigma_n = 1.56$. Hence observations made close together have less individual weight than well-separated observations.

The second sum of (A9) is only over those times when the barotropic model control variables are defined ($\kappa(0)=1$ in (A5)) to avoid summing over the time interpolation weights. It measures two properties of the barotropic model state that we choose also to minimize. Vorticity $\zeta_{i,j}^t = u_{i+1,j+1}^t - u_{i,j+1}^t + v_{i+1,j+1}^t - v_{i+1,j}^t$ is penalized only at interior grid points (to avoid adding extra terms to (A15) but volume flux is penalized at all grid points. Note that we use the same symbol h for the bathymetry estimated at the u, v, and p grid points. The estimated variances of the barotropic vorticity and volume flux are denoted by σ_ζ^2 and σ_v^2, respectively.

The third sum is only over the geostrophic model control times (for reasons as above) and penalizes the geostrophic velocity evaluated at a grid of locations spanning the domain of the barotropic model. The estimated variance is σ_u^2.

The last sum of (A9) simply keeps the pressure offsets $\bar{p}$ clustered about zero.

The Adjoint Method

We wish to minimize J subject to the strong constraint that p, u, and v obey the discretized forms of (A2-A4). We do this by adding to J the left-hand side of (A2-A4), multiplied by a set of undetermined Lagrange multipliers (P, U, and V) for every time step and grid point to form the Lagrangian

$$L = J + \sum_{t=1}^{N} \Bigg\{$$

$$\sum_{i=1}^{n}\sum_{j=1}^{m} P_{i,j}^t \left[p_{i,j}^{t+1} - p_{i,j}^t + c^2 \Delta t \left(\frac{h_{i,j+1} u_{i,j+1}^t - h_{i,j} u_{i,j}^t}{\Delta x} \right.\right.$$

$$\left.\left. + \frac{h_{i,j} v_{i,j}^t - h_{i+1,j} v_{i+1,j}^t}{\Delta y} \right) \right]$$

$$+ \sum_{i=1}^{n}\sum_{j=2}^{m} U_{i,j}^t \left(\frac{u_{i,j}^{t+1} - u_{i,j}^t}{\Delta t} + \frac{p_{i,j}^{t+1} - p_{i,j-1}^{t+1}}{\Delta x} \right.$$

$$\left. - \frac{v_{i,j}^t + v_{i+1,j}^t + v_{i,j-1}^t + v_{i+1,j-1}^t}{4F} + \frac{C_d v^* u_{i,j}^t - \tau^x}{h_{i,j}} \right)$$

$$+ \sum_{i=2}^{n}\sum_{j=1}^{m} V_{i,j}^t \left(\frac{v_{i,j}^{t+1} - v_{i,j}^t}{\Delta t} + \frac{p_{i-1,j}^{t+1} - p_{i,j}^{t+1}}{\Delta y} \right.$$

$$\left. + \frac{u_{i,j}^t + u_{i-1,j}^t + u_{i,j+1}^t + u_{i-1,j+1}^t}{4F} + \frac{C_d v^* v_{i,j}^t - \tau^y}{h_{i,j}} \right) \Bigg\}$$

$$(A11)$$

and then seek the point at which all derivatives of L are zero [*Thacker*, 1987]. Differentiating with respect to P, U, and V returns the original model equations, while differentiating with respect to p, u, and v yields a set of time-stepping equations for P, U, and V (which are sometimes called the backward model because they are integrated in reverse, starting with $P = U = V = 0$ at $t = N$). Setting $\partial L/\partial u_{i,j}^t = 0$ for $i = 1..n$, $j = 2..m$ and $t = 1..N$ yields

$$U_{i,j}^{t-1} = U_{i,j}^t - \Delta t \left(\frac{V_{i,j}^t + V_{i+1,j}^t + V_{i,j-1}^t + V_{i+1,j-1}^t}{4F} \right.$$

$$\left. + c^2 h_{i,j} \Delta t \frac{P_{i,j-1}^t - P_{i,j}^t}{\Delta x} + \frac{C_d v^* U_{i,j}^t}{h_{i,j}} + \frac{\partial J}{\partial u_{i,j}^t} \right) \quad (A12)$$

where

$$\frac{\partial J}{\partial u_{i,j}^t} = -\sum_{k=1}^{n_u^t}\sum_{l=1}^{n_u^t} \frac{\psi_{k,l}^t}{2} \Big[\beta(\mathbf{x}_k^t - \mathbf{x}_{i,j})(\tilde{u}_l^t - u_l^t)$$

$$+ (\tilde{u}_k^t - u_k^t)\beta(\mathbf{x}_l^t - \mathbf{x}_{i,j}) \Big]$$

$$+ \frac{\delta\zeta_{i-1,j-1}^t - \delta\zeta_{i,j-1}^t}{\sigma_\zeta^2} + \frac{\delta h_{i,j}^2 u_{i,j}^t}{\sigma_v^2} \quad (A13)$$

provides forcing terms proportional to model velocity errors, vorticity and transport at the times and places (where $\delta = 1$, otherwise $\delta = 0$) that these quantities contribute to J. The effects of these forcings propagate backward through the adjoint model dynamics, eventually reaching the boundary and/or initial conditions.

Note that the last term of (A13) requires the fields of the forward model to be stored at control time steps for use by the adjoint model. Similarly, the v^* field used in the forward model must also be available to the adjoint model.

The equation for V is derived similarly and is omitted here. Setting $\partial L/\partial p^t_{i,j} = 0$ for $i = 1..n$, $j = 1..m$ and $t = 1..N$ yields

$$P^{t-1}_{i,j} = P^t_{i,j} - \frac{U^{t-1}_{i,j} - U^{t-1}_{i,j+1}}{\Delta x} - \frac{V^{t-1}_{i+1,j} - V^{t-1}_{i,j}}{\Delta y}$$

$$- \frac{\partial L}{\partial u^t_{i,j}}\frac{\partial u^t_{i,j}}{\partial p^t_{i,j}} + \sum_{k=1}^{n^t_p}\frac{\beta^t_k(\tilde{p}^t_k - p^t_k)}{\sigma^2_p}$$

$$+ \sum_{k=2}^{n^t_p}\frac{(\beta^t_k - \beta^t_1)\left[(\tilde{p}^t_k - \tilde{p}^t_1) - (p^t_k - p^t_1)\right]}{\sigma^2_{\Delta p}} \quad (A14)$$

where, at the left boundary, for example,

$$\frac{\partial L}{\partial u^t_{i,1}} = \frac{V^t_{i,1} + V^t_{i+1,1}}{4F} - c^2 h_{i,1}\Delta t\frac{P^t_{i,1}}{\Delta x} + \frac{\delta h^2_{i,1}u^t_{i,1}}{\sigma^2_v} \quad (A15)$$

(here $\delta = 1$ at the control times of the barotropic model, otherwise $\delta = 0$, see (A9)) and $\partial u/\partial p$ would be zero if it were not for our inclusion of the gravity-wave-radiating component in (A5), which leads to

$$\frac{\partial u^t_{i,1}}{\partial p^t_{i,1}} = -\frac{\cos\theta}{c\sqrt{h_{i,1}}} \quad (A16)$$

being nonzero. Note that $P^{t-1}_{i,j}$ is in terms of $U^{t-1}_{i,j}$ and $V^{t-1}_{i,j}$, so the latter have to be calculated first, in reverse order to the forward model, which first updates the pressure.

Gradient of J With Respect to the Control Variables

To recognize the physical interpretation of the adjoint model, note that the only appearance of $p^1_{i,j}$ in (A11) is in the $P^1_{i,j}$ term, so $\partial L/\partial p^1_{i,j} = -P^1_{i,j}$; that is, the values of the Lagrange multipliers for p at the end of the backward integration indicate how the initial pressure field of the model needs to be altered to minimize J. To evaluate $\partial L/\partial u^1_{i,j}$, it is simplest to define an extra field of Lagrange multipliers for $t = 0$ and then $\partial L/\partial u^1_{i,j} = -U^0_{i,j}/\Delta t$.

For our application we wish to compute the derivative of J (and hence L [Thacker, 1987]) with respect to the boundary flows, which we have parameterized according to (A5). For the left boundary, $\partial L/\partial l^T_s$ has terms of the form $\partial L/\partial u \; \partial u/\partial l^T_s$ so

$$\frac{\partial L}{\partial l^T_s} = \sum_{i=1}^{n}\chi_{s,i}\sum_{t=1}^{N}\frac{\kappa(t-T)}{h_{i,1}}\frac{\partial L}{\partial u^t_{i,1}}. \quad (A17)$$

The other type of control variable for the barotropic model is the mean pressure $\bar{p}_k$ at each gauge. The gradient

$$\frac{\partial L}{\partial \bar{p}_k} = -\sum_{t=1}^{N}\left[\sum_{k=1}^{n^t_p}\frac{\tilde{p}^t_k - p^t_k}{\sigma^2_p} + \sum_{k=2}^{n^t_p}\frac{(\tilde{p}^t_k - \tilde{p}^t_1) - (p^t_k - p^t_1)}{\sigma^2_{\Delta p}}\right]$$

$$+ \frac{\bar{p}_k}{\sigma^2_p} \quad (A18)$$

follows directly from (A9).

For the geostrophic model component, the gradient

$$\frac{\partial L}{\partial \alpha^T_s} = F\sum_{t=1}^{N}\omega(t-T)\left\{\sum_{k=1}^{n^t_u}\sum_{l=1}^{n^t_u}\frac{\psi^t_{k,l}}{2}\left[\frac{\partial\phi_s}{\partial y}\bigg|_k(\tilde{u}^t_l - u^t_l)\right.\right.$$

$$\left.+(\tilde{u}^t_k - u^t_k)\frac{\partial\phi_s}{\partial y}\bigg|_l - \frac{\partial\phi_s}{\partial x}\bigg|_k(\tilde{v}^t_l - v^t_l) - (\tilde{v}^t_k - v^t_k)\frac{\partial\phi_s}{\partial x}\bigg|_l\right]\right\}$$

$$+ \frac{F}{\sigma^2_u}\sum_{i=1}^{n}\sum_{j=1}^{m}\left(\dot{v}^t_{i,j}\frac{\partial\phi_s}{\partial x}\bigg|_{i,j} - \dot{u}^t_{i,j}\frac{\partial\phi_s}{\partial y}\bigg|_{i,j}\right) \quad (A19)$$

also follows directly from (A9) because (A6) is easily differentiable. The last term is outside the sum over t because the transport is only penalized at control times.

It is, of course, very easy to make an error programming the forward and backward models, which, if small, may be mistaken for ill conditioning of the problem. TG describe how we verify that the computed gradients are correct to machine accuracy.

References

Bowen, A. J., D. A. Griffin, D. G. Hazen, S. A. Matheson, and K. R. Thompson, Ship-board nowcasting of shelf circulation, *Cont. Shelf Res.*, *15*, 115-128, 1995.

Brander, K. M., and P. C. Hurley, Distribution of early-stage Atlantic cod (Gadus morhua), haddock (Melanogrammus aeglefinus), and witch flounder (Glyptocephalus cynoglossus) eggs on the Scotian Shelf; A reappraisal of evidence on the coupling of cod spawning and plankton production, *Can. J. Fish. Aquat. Sci.*, *49*, 238-251, 1992.

Chapman, D. C., Numerical treatment of cross-shelf open boundaries in a barotropic coastal ocean model, *J. Phys. Oceanogr.*, *15*, 1060-1075, 1985.

Chavent, G., M. Dupuy, and P. Lemonnier, History matching by use of optimal theory, *Soc. Pet. Eng. J.*, *15*, 74-86, 1975.

Das, S. K., and R. W. Lardner, On the estimation of parameters of hydraulic models by assimilation of periodic tidal data, *J. Geophys. Res.*, *96*, 15,187-15,196, 1991.

Farrell, B. F., and A. M. Moore, An adjoint method for obtaining the most rapidly growing perturbation to oceanic flows, *J. Phys. Oceanogr.*, *22*, 338-349, 1992.

Gentry, R. A., R. E. Martin, and B. J. Daly, An Eulerian differencing method for unsteady compressible flow problems, *J. Comput. Phys.*, *1*, 87–118, 1966.

Ghil, M., and P. Malanotte-Rizzoli, Data assimilation in meteorology and oceanography, *Adv. Geophys.*, *33*, 141–265, 1991.

Gill, P., W. Murray, and M. Wright, *Practical Optimization*, Academic, San Diego, Calif., 1981.

Heemink, A. W., and I. D. M. Metzelaar, Data assimilation into a numerical shallow water flow model: A stochastic optimal control approach, *J. Mar. Syst.*, *6*, 145–158, 1995.

Kamarchi, M., and J. J. O'Brien, Continuous data assimilation of drifting buoy trajectory into an equatorial Pacific Ocean model, *J. Mar. Syst.*, *6*, 159–178, 1995.

Lardner, R. W., Optimal control of open boundary conditions for a numerical tidal model, *Comput. Methods Appl. Mech. Eng.*, *102*, 367–387, 1993.

Lardner, R. W., A. H. Al-Rabeh, and N. Gunay, Optimal estimation of parameters for a two-dimensional hydrodynamical model of the Arabian Gulf, *J. Geophys. Res.*, *98*, 18,229–18,242, 1993.

Large, W. S., and S. Pond, Open ocean momentum flux in moderate to strong winds, *J. Phys. Oceanogr.*, *11*, 324–336, 1981.

Moore, A. M., Data assimilation in a quasi-geostrophic open-ocean model of the Gulf Stream region using the adjoint method, *J. Phys. Oceanogr.*, *21*, 398–427, 1991.

Moore, A. M., and B. F. Farrell, Rapid perturbation growth on spatially and temporally varying oceanic flows determined using an adjoint method: Application to the Gulf Stream, *J. Phys. Oceanogr.*, *23*, 1682–1702, 1993.

Nechaev, D. A., and M. I. Yaremchuk, Conductivity-temperature-depth data assimilation into a three-dimensional quasi-geostrophic open ocean model, *Dyn. Atmos. Oceans*, *21*, 137–165, 1994.

O'Boyle, R. M., M. Sinclair, R. J. Conover, K. H. Mann, and A. C. Kohler, Temporal and spatial distribution of ichthyoplankton communities of the Scotian Shelf in relation to biological, hydrological, and physiographic features, *Rapp. P.V. Reun. Cons. Int. Explor. Sci. Mer Mediter.*, *183*, 27–40, 1984.

Panchang, V. G., and J. J. O'Brien, On the determination of hydraulic model parameters using the adjoint state formulation, in *Modelling Marine Systems*, edited by A. M. Davies, pp. 6–18, CRC Press, Boca Raton, Fla., 1989.

Pollard, R. T., and R. C. Millard, Comparison between observed and simulated wind-generated inertial oscillations, *Deep Sea Res.*, *17*, 813–821, 1970.

Reid, R. O., and B. R. Bodine, Numerical model for storm surges in Galveston Bay, *J. Waterw. Harbors Coastal Eng. Div. Am. Soc. Civ. Eng.*, *94*(WW1), 33–57, 1968.

Røed, L. P., and C. Cooper, A study of various open boundary conditions for wind-forced barotropic numerical ocean models, in *Three-Dimensional Models of Marine and Estuarine Dynamics*, edited by J. C. J. Nihoul, and B. M. Jamart, pp. 305–335, Elsevier, New York, 1987.

Sameoto, D., L. Jaroszynski, and W. Fraser, BIONESS, a new design in multiple net zooplankton samplers, *Can. J. Fish. Aquat. Sci.*, *37*, 722–724, 1980.

Sanderson, B., Structure of an eddy measured with drifters, *J. Geophys. Res.*, *100*, 6761–6776, 1995.

Sasaki, Y., Some basic formalisms in numerical variational analysis, *Mon. Weather Rev.*, *98*, 875–883, 1970.

Schiller, A., The mean circulation of the Atlantic ocean north of 30S determined with the adjoint method applied to an ocean general circulation model, *J. Mar. Res.*, *53*, 453–497, 1995.

Schlitzer, R., Determining the mean, large-scale circulation of the Atlantic with the adjoint method, *J. Phys. Oceanogr.*, *23*, 1935–1952, 1993.

Seiler, U., Estimation of open boundary conditions with the adjoint method, *J. Geophys. Res.*, *98*, 22,855–22,870, 1993.

Smedstad, O. M., and J. J. O'Brien, Variational data assimilation and parameter estimation in an equatorial Pacific Ocean model, *Prog. Oceanogr.*, *26*, 179–241, 1991.

Taggart, C. T., S. E. Lochmann, D. A. Griffin, and K. R. Thompson, Abundance distribution of larval cod (Gadus morhua) and zooplankton in a gyre-like water mass on the Scotian Shelf, in *Survival Strategies in Early Life Stages of Marine Resources. Proc. Internat. Workshop, Yokohama, 11-14 October 1994*, edited by Y. Watanabe, Y. Yamashita, and Y. Oozeki, pp. 127–145, Balkema Press, Rotterdam, 1995.

Talagrand, O., and P. Courtier, Variational assimilation of meteorological observations with the adjoint vorticity equation, I, theory, *Q. J. R. Meteorol. Soc.*, *113*, 1311–1328, 1987.

Thacker, W. C., Three lectures on fitting numerical models to observations, *Rep. GKSS 87/E/65*, GKSS Forschungszentrum Geesthacht GmbH, Geesthacht, Germany, 1987.

Thacker, W. C., Fitting models to data by enforcing spatial and temporal smoothness, *J. Geophys. Res.*, *93*, 10,655–10,665, 1988.

Thacker, W. C., and R. B. Long, Fitting dynamics to data, *J. Geophys. Res.*, *93*, 1227–1240, 1988.

Tziperman, E., W. C. Thacker, R. B. Long, and S.-M. Hwang, Oceanic data analysis using a general circulation model, I, Simulations, *J. Phys. Oceanogr.*, *22*, 1434–1457, 1992a.

Tziperman, E., W. C. Thacker, R. B. Long, S.-M. Hwang, and S. R. Rintoul, Oceanic data analysis using a general circulation model, II, A North Atlantic model, *J. Phys. Oceanogr.*, *22*, 1458–1485, 1992b.

Vogeler, A., and J. Schröter, Assimilation of satellite altimeter data into an open ocean model, *J. Geophys. Res.*, *100*, 15,951–15,963, 1995.

Zou, X., I. M. Navon, and F. X. L. Dimet, Incomplete observations and control of gravity waves in variational data assimilation, *Tellus, Ser. A*, *44A*, 273–296, 1992.

D.A. Griffin, Division of Oceanography, Commonwealth Scientific and Industrial Research Organisation, GPO Box 1538, Hobart, Tasmania 7001, Australia. (e-mail: griffin@ml.csiro.au)

K.R. Thompson, Oceanography Department, Dalhousie University, Halifax, Nova Scotia B3H4J1, Canada. (e-mail: keith@phys.ocean.dal.ca)